# Chapter 1 Introduction

The applications of semiconductor laser diodes are more important day by day since semiconductor laser diodes were first demonstrated in the early 1960's. They are used in widely applications such as readout source in optical disk media, biological detection, display, optical fiber communication and optical computing, etc., due to the advantages of considerably smaller size, higher efficiency with lower power requirements, long lifetime, and the ability to be modulated optical output to a few GHz with a simple driving circuit.

Classified according to the resonant direction of stimulated emission light, there are tow types of laser diodes. The resonant direction of the edge emitting laser (EEL) is horizontal to the epitaxial direction of the laser structure. On the contrary, the resonant direction of the vertical-cavity surface-emitting laser (VCSEL) is vertical to the epitaxial direction of the laser structure. Between two types of laser diodes, the properties of circular emitting pattern, low threshold current, 2-D array package, on-wafer test, etc. give VCSEL superiority over EEL. High efficiency in fiber coupling due to circular emitting pattern also makes the VCSEL be seen as a highly potential source in the optical fiber communication systems.

In recently years, the worldwide interest in optical-fiber communications has moved very rapidly from system using a wavelength of about 0.85μm to those using 1.3 or 1.55 μm ( called as 'long wavelength'), because of the greater repeaterless system lengths and/or bandwidth which LW-VCSELs offer. In an optical communication system, information is transmitted by light propagation inside an

optical fiber in the form of a coded sequence of optical pulses. The signal weakens during propagation because of the fiber loss. After traveling some distance, the traveling light needs to be regenerated with a repeater. System cost considerations require that the repeaters spacing, L, should be as large as possible. Another consideration is the bite rate, B (number of bits transmitted per second), which determines the transmission capacity. An important issue of the optical transmission system is to maximize the bit rate-distance product, BL. The bit rate is limited by chromatic dispersion in optical fiber, which causes broadening of optical pulses during the pulses propagate in optical fiber. The choice of the operating wavelength is therefore related to the loss and dispersion characteristics of the fiber. Fig. 1.1 and Fig. 1.2 show the optical loss (dB/km) and the dispersion coefficient [ps/(km.nm) ] as functions of the wavelength for typical single-mode silica fibers. As illustrated in Fig. 1.1, minimum fiber loss occurs around 1.55 μm. At this wavelength the repeater spacing can easily exceed 100km for moderate bit rates. At high bit rates (B≧1Gb/s) the repeater spacing is limited not only by the fiber loss but rather by the extent of fiber dispersion.

However, there are some problems in fabricating long wavelength vertical cavity surface emitting laser (LW-VCSEL). In a mature and general used fabrication process of the VCSEL, the bottom distributed Bragg reflectors (DBR) was first deposited on the substrate and followed by an active region, then the top DBR. In the epitaxial process, lattice matching is necessary to avoid defects which can destroy the proper operation of diode lasers. The realization of the practical 1.3 and 1.55 mm VCSEL was then primarily hindered by the fact that the conventional choice for the fabrication of the laser mirrors is the InGaAsP quaternary alloy lattice matched to InP. The difficulty with this material system lies in the relatively small range of refractive

indexes that can be achieved by varying the composition of this alloy while lattice matched to InP [1.1]. The refractive index difference and material absorption directly influences the ability to realize high reflectivity DBR. Furthermore, the thermal conductivity of InGaAsP is an order of magnitude smaller than that of InP due to the alloy scattering [1.1]. The lack of suitable epitaxial mirrors for both sides of the resonator has led to the development of amorphous dielectric mirrors deposited by various low temperature deposition techniques [1.2, 1.3]. These mirrors can be fabricated to have very high reflectivity, but are nonconductive and typically thermally insulating.

One of the promising methods for realization of practical room-temperature operating LW-VCSELs is *wafer fusion* [1.5, 1.6]. In this method, substrates of vastly different lattice constants (InP and GaAs) are fused to produce an electrically and optically transparent junction [1.7]. The optical and thermal properties of the binary AlAs/GaAs mirrors are substantially better than amorphous dielectric and InGaAsP/InP mirrors. This leads to the successful demonstration for the vertical-cavity lasers and resonant-cavity photodetectors fabricated by combining the InP based active layers with a single GaAs/AlAs mirror [1.4, 1.8]. The purposes of this research are to systematically establish the wafer fusion techniques for fabrication of LW-VCSEL. In chapter 2, the operation principles of VCSEL will be introduced. Then, the experimental setup, fusion techniques and the optimization process for the fusion will be presented in chapter 3. Next, chapter 4 includes the design rules and simulation results for the wafer-fused LW-VCSELs. Experimental results are presented and discussed in chapter 5. Finally, chapter 6 is the conclusion to this study.
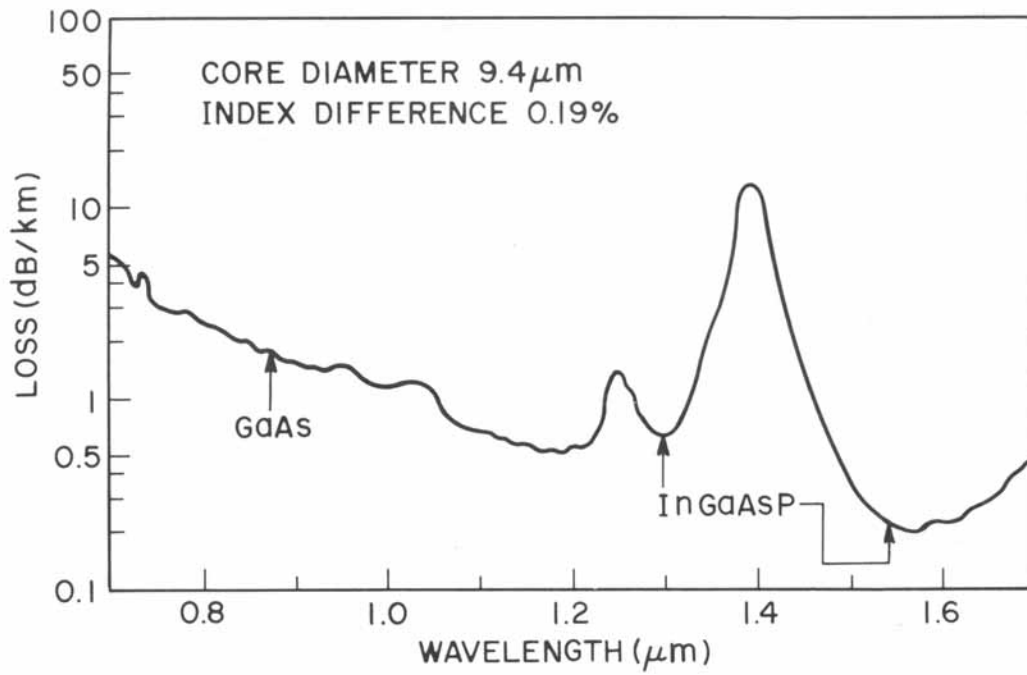
**Fig. 1.1** Measured loss for typical single-mode silica fibers.
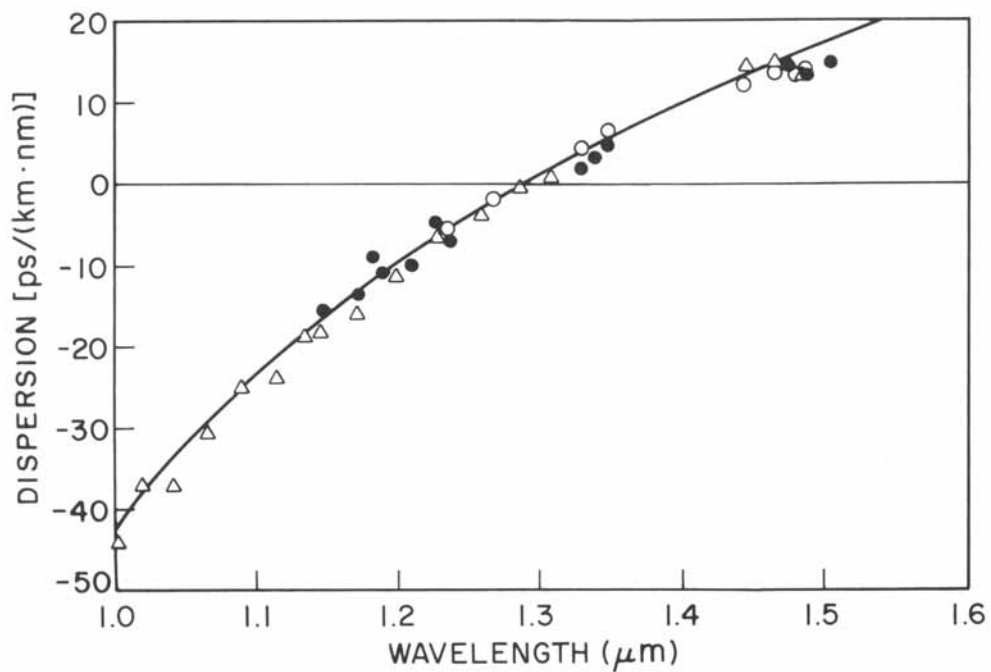


**Fig. 1.2** Measured material dispersion for typical single-mode silica fibers.

# Chapter 2 The operation principles of VCSELs

## 2.1 Ingredients of the laser

The word LASER is an acronym for **L**ight **A**mplification by **S**timulated **E**mitting of **R**adiation. To form the "laser", there are three ingredients:

**(1) *Gain medium:*** The gain medium consisting of a material which normally absorbs incident radiation over some wavelength range of interest. But, if it is pumped by inputting either electrical or optical energy, the electrons within the material can be excited to the higher, nonequilibrium energy level, so that the incident radiation can be amplified rather than absorbed by stimulating the de-excitation of these electrons along with the generation of additional radiation. If the resulting gain is sufficient to overcome the losses of some resonant optical mode of the cavity, this mode is said to have reached threshold, and relatively coherent light will be emitted.

**(2) *Pumping source:*** Pumping source provides the energy that can excite the electrons within gain medium at lower energy level to higher energy level. It could be either optical or electrical energy.

**(3) *Resonant cavity:*** The resonant cavity provides the necessary positive feedback for the radiation being amplified, so that a lasing oscillation can be established and sustained above threshold pumping level.

Some basic concepts that relate to these three ingredients and that are needed to understand the semiconductor laser diodes will be introduced in the following sections.

## 2.2 Energy bands in the solids

Fig. 2.1 illustrates two discrete energy levels of an atom and the energy bands of a solid [2.1]. The reason that two discrete energy level of an atom develop into bands of a solid can be realized as follows. When two atoms are in close proximity, the outer valence electron of one atom can arrange itself into a low-energy bonding distribution or a high-energy anti-bonding. Therefore the isolated energy level of the electron is now split into two levels due to the two ways the electron can arrange it self around the two atoms.

If another atom is brought together with the first two atoms, a new charge distribution is possible that is neither completely bonding nor anti-bonding. Hence a third energy level is formed. When N atoms are covalently bonded into a linear chain, N energy levels distributed between the lowest-energy bonding state and highest-energy anti-bonding state forming a band of energies.

The semiconductor valence band is formed by the multiple splitting of the highest occupied atomic energy level of the constituent atoms. In semiconductors, the valence band is by definition entirely filled with no external excitation at T=0 K. Likewise, the next higher atomic level splits apart into the conduction band which is entire empty in semiconductors without any excitation. With energy is added to the system, electrons in the valence band may be excited to the conduction band. The excitation creates holes in the valence band as well as electrons in the conduction band, and both contribute to conduction.

Fig. 2.1 suggests that many conduction-valence band state pairs may interact with photons of energy $E_{21}$. But in real case, besides the conservation of energy, the

conservation of momentum must be considered during transition process. This situation can be illustrated by electron energy vs. k-vector plot shown as Fig. 2.2. Since the momentum of interacting photon is negligibly small compared to the electron, transition between conduction and valence band must have the same k vector.

## 2.3 The creation of light

We proceed to consider the electron transitions that can exist and the interactions with lightwaves that are possible. Fig.2.3 illustrates three different kinds of electrons transitions that involve the absorption or emission of photons [2.2].
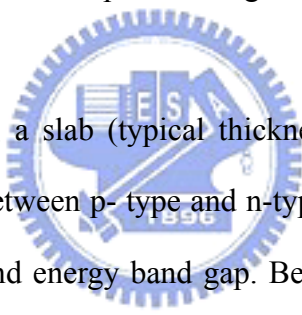
Four basic recombination / generation mechanisms can be considered as follows.

(1) *Spontaneous emission:* An electron in conduction band recombines spontaneously with a hole in the valence band to generate a photon. If a large number of such events occur, incoherent emission would occur due to the emission time and directions are random.

(2) *Stimulated absorption:* An electron in the valence band absorbs a photon and transits to the conduction band while leaving a hole in the valence band.

(3) *Stimulated emission:* An incident photon stimulates the recombination of an electron and a hole, and subsequently generating a photon. This is the most important positive gain mechanism for lasers to operation. The stimulated photon is identical with the incident photon in frequency, direction of propagation, state of polarization, and phase.

(4) *Nonradiative recombination:* Instead of generating a photon, a conduction band electron recombines with a valence band electron, and dissipating the energy as heat in the crystal. There are two general nonradiative recombination for carriers

that are important. One involves nonradiative recombination centers, such as point defects, interfaces in the active region of the laser. Another is the Auger recombination, in which electron-hole recombination energy, is given to another electron or hole in the form of kinetic energy.

## 2.4 The double heterostructures

As mentioned in section 2.1, the active region (gain medium) must be pumped with an external energy source. A major superiority of diode laser is their ability to be pumped by electrical current. In Fig. 2.4, a schematic of broad-area p-i-n double heterostructure (DH) laser diode, along with transverse sketches of the energy gap, index of refractivity, and optical mode profile are given [2.3].

As shown in Fig. 2.4(a), a slab (typical thickness is 0.1~0.2 μm) of undoped active region is sandwiched between p- type and n-type cladding layers which have a higher conduction-valence band energy band gap. Because the band gap of cladding layers is larger, light generated in the active region will not be absorbed by them. For this DH structure, electrons and holes are injected from n- and p- type regions, respectively, under forward bias. Then electrons and holes are confined together in the active region, subsequently increasing the recombination probability of electron-hole pairs.

The necessary resonant cavity for optical feedback can be formed with cleaved facets, since the cleaved facet-air interface can provide a reflectivity of ~ 30%. In III-V materials, the materials with lower energy band gap usually have higher refractive index. Therefore, as shown in Fig. 2.4(c), a transverse optical waveguide is formed automatically, with its axis along the z- direction. The transverse optical

energy density profile ( proportional to electrical field magnitude squared, $|E|^2$ ) is illustrated as Fig. 2.4(d).

Then, with injected electrons and holes, stimulated and amplified photons in active region and optical feedback provided by cleaved facets, the stimulated emission are formed in this DH structure.

## 2.5 Semiconductor materials for laser diodes

The properties of the material which used in laser structure are the key issue in the fabrication of a laser diode. The most fundamental requirement for these different materials is that the same crystal structure and nearly the same lattice constant, so that, single crystal, defect free films of one can be epitaxially grown on the other.
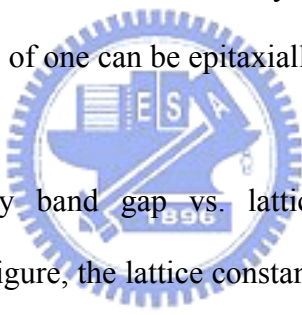
Fig.2.5 plots the energy band gap vs. lattice constant for several III-V compounds. As illustrated in figure, the lattice constant of InP and GaAs is 5.86Å and 5.65Å, respectively. It is well known that a small lattice mismatch (Δa/a~1%, "a" is lattice constant and "Δa" is the different of lattice constant between the two materials) can be tolerated up to the critical thickness of about 20nm without any defect. The Δa/a ratio of InP/GaAs is about 3%, thereby the critical thickness must be thinner than 20nm. The thin thickness limits probable application of GaAs epitaxial growth on InP. In this thesis, wafer fusion technique is used to overcome the lattice-mismatched problem.

## 2.6 Operation mechanisms of VCSELs

The operation of a VCSEL, like other diode laser, can be understood by observing the flow of carriers into active region, the generation of photons due to the

recombination of some of these carriers and transmission of some of these photons out of the optical cavity. The dynamics can be described by a set of rate equations. Consider the general VCSEL structure as shown in Fig. 2.6. The radius of active region is a. The active region length and effective cavity length is $L_a$ and L respectively. Assume the hole density is equal to electron density ( N ). For simplicity, one photon density ( $N_p$ ) for one output mode is also assumed.

The rate equations can be written as follows:

$$\frac{dN}{dt} = \eta_i \frac{I}{qV} - R_{sp} - R_{nr} - g\, v_g\, N_p \qquad (2.1)$$

and

$$\frac{dNp}{dt} = \Gamma\, g\, v_g\, N_p + \Gamma\, \beta_{sp}\, R_{sp} - \frac{N_p}{\tau_p} \qquad (2.2)$$

where the injection efficiency $\eta_i$ is the ratio of carries that recombine in the active region to the terminal injection carriers; I is the terminal injection current; q is electron charge; $V = \pi a^2 L_a$ is volume of active region; $R_{sp}$ is the spontaneous recombination rate; $R_{nr}$ is the nonrecombination rate; $gv_gN_p$ is the stimulated recombination rate where g is optical gain of active material and $v_g$ is the group velocity in the axial direction of the mode in equation; $\Gamma$ is confinement factor; $\beta_{sp}$ is the spontaneous emission factor; and $\tau_p$ is the photon life time in the cavity.

In equation (2.1), left hand side of equal sign is the generation rate of carrier. In the right hand side, the first term is the generation rate of carrier and the second, third and fourth terms are the generation rates of photon. In equation (2.2), left hand side of equal sign is the rate of photon. In the right hand side, the first term is the generation rate of photon by stimulated emission and the second term is the generation rate of

photon which contributed by spontaneous emission. The fourth term is photon loss rate caused by output photons.

The cavity lifetime $\tau_p$ is given by the optical losses in the cavity,

$$\frac{1}{\tau_p} = v_g (\alpha_i + \alpha_m) \tag{2.3}$$

where $\alpha_i$ is the internal power loss and $\alpha_m = (1/L) \ln(1/R)$ is mirror loss. The mean mirror power reflection coefficient is $R = |r_1 r_2|$, where $r_1$ and $r_2$ are the amplitude reflection coefficients for the two mirrors.

Therefore, the threshold gain in the steady state can be presented with following equation,

$$\Gamma g_{th} = \frac{1}{v_g \tau_p} = \alpha_i + \alpha_m = \alpha_i + \frac{1}{L} \ln(\frac{1}{R}) \tag{2.4}$$
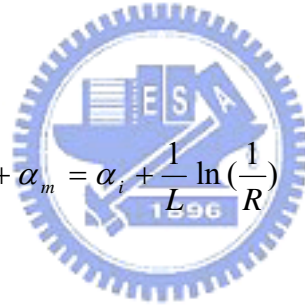
Note that the photon decay rate, $1/\tau_p = 1/\tau_i + 1/\tau_m$ where $\tau_i$ and $\tau_m$ are photon life time related to internal loss and mirror loss respectively.

## 2.7 Output power versus driving current

Under steady state, ( $dN/dt=0$ ), and as the current just arrive at threshold current ( the value to obtain $g_{th}$ ), we can set $g v_g N_p = 0$. Then $R_{sp} + R_{nr} = \eta_i I_{th}/qV$ ( $I > I_{th}$ )can be obtained. Now equation (2.1) can be rewritten as:

$$\frac{dN}{dt} = \eta_i \frac{(I - I_{th})}{qV} - g v_g N_p . \tag{2.5}$$

When the current is above $I_{th}$ and under steady state, $N_p$ multiplied by volume of the

active region, the photon energy hν, the loss rate out of the mirrors, $v_g\alpha_m$, the power coupling output of the mirrors is

$$P_o = \frac{h\nu}{q}\eta_d(I - I_{th}),$$  (2.6)

Where the differential efficiency is

$$\eta_d = \eta_i \frac{\alpha_m}{\alpha_i + \alpha_m}.$$  (2.7)

Though thermal effect, mode hopping and other effects may affect the output power, the L-I (light output power-current) curve is basically governed by equation 2.6.

## 2.8 The VCSELs fabricated with wafer fusion technique

In equation (2.4), it is clear that in order to reduce the threshold gain, high reflectivity DBR in a VCSEL structure are necessary. The reflectivity of the DBR in a VCSEL is usually higher than 99.5%. As mentioned in chapter 1, the realization of practical 1.3 and 1.55 mm VCSEL is primarily hindered by the fact that the present choice for the fabrication of the laser mirrors is the InGaAsP quaternary alloy lattice matched to InP. The difficulty with this material system lies in the relatively small range of refractive indexes that can be achieved by varying the composition of this alloy while lattice matched to. On the contrary, high refractive index difference between GaAs and AlAs and non-absorption of these two materials for 1.3~1.5 nm wavelength make integration of InP based material and GaAs/AlAS DBR a candidate for solving the problem. GaAs and AlAs also have higher thermal conductivity than InGaAsP. When a VCSEL is operating, heat produced by resistance of component effects the characteristics of VCSEL a lot. The heat which does not transmit to heat

sink remains in the device induce increasing of threshold gain, decreasing out put power, mode hopping and low reliability.

Table 1.1 shows the optical and thermal comparison between GaAS/AlAs and InP/InGaASP DBRs [2.4, 2.5]. 47 pairs of InP/InGaAsP DBR is required to achieve a reflectivity in excess of 99.5%. Such a large number of pairs is a challenge of uniform epitaxial growth and growth time. The thermal conductivity of GaAs is higher than InGAAsP of one order. In this thiese, wafer fusion technique is used to integrate lower pairs and higher thermal conductivity GaAs.AlAs DBR with InP based gain materials. The band gaps of GaAs and AlAs are 1.42eV and 2.15 eV which do not absorb the light with 1300~1500nm. It is important that the DBR materials don't absorb the emission light from active region.

| DBR materials | $\triangle n$ | Number of DBR pairs for R=99.5% | Thermal conductivity (W/m$^{-1}$K$^{-1}$) | Band gap (eV) |
|---|---|---|---|---|
| GaAs/AlAs | 0.43 | **25** | GaAs = 46 | 1.42/2.15 |
| InP/InGaAsP | 0.27 | **47** | InGaAsP = 4.2 | 1.35/0.8-0.95 |

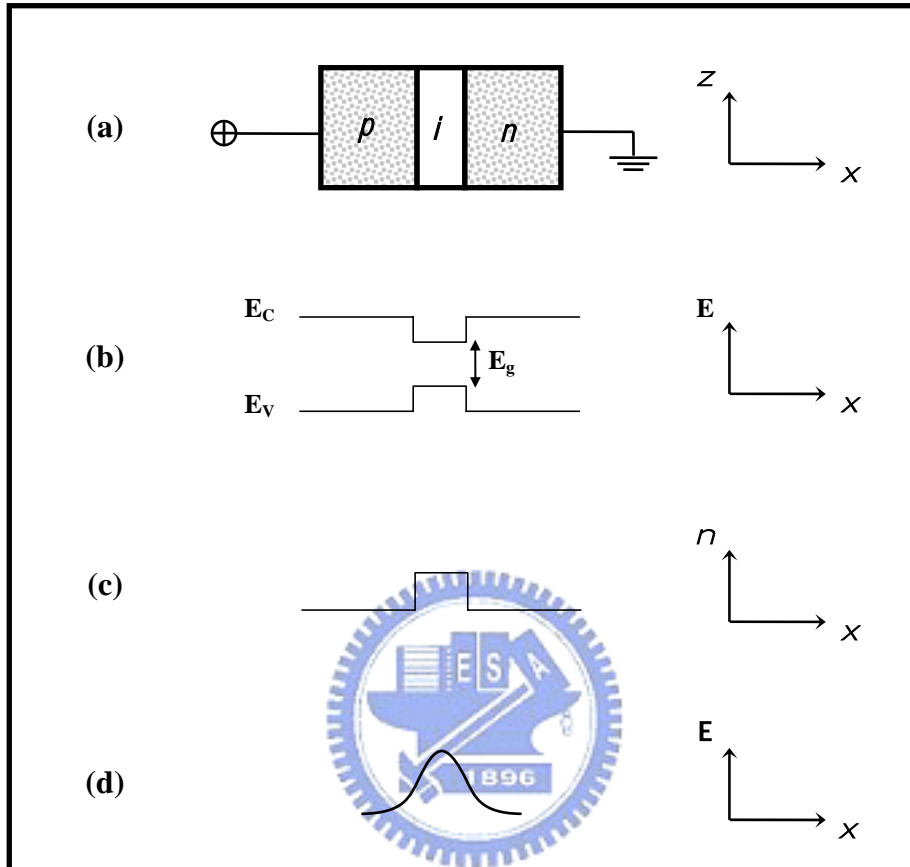**Table 2.1** The numer of pair for reflectivity=99.5% and thermal conductivity of GaAs/AlAs and InP/InGaAsP DBRs
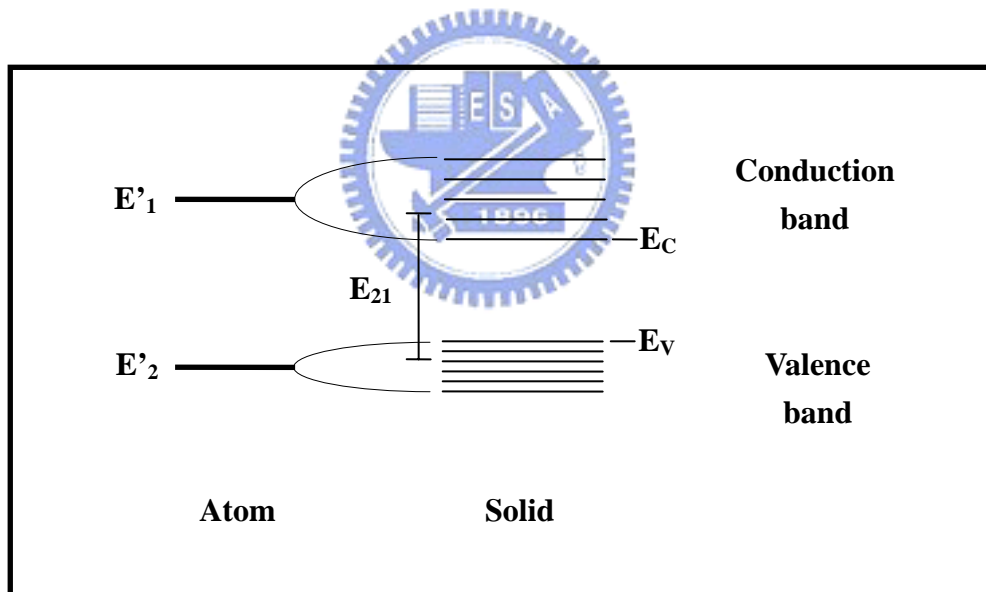


**Fig. 2.1** Two discrete energy level of an atom and the energy bands of a solid
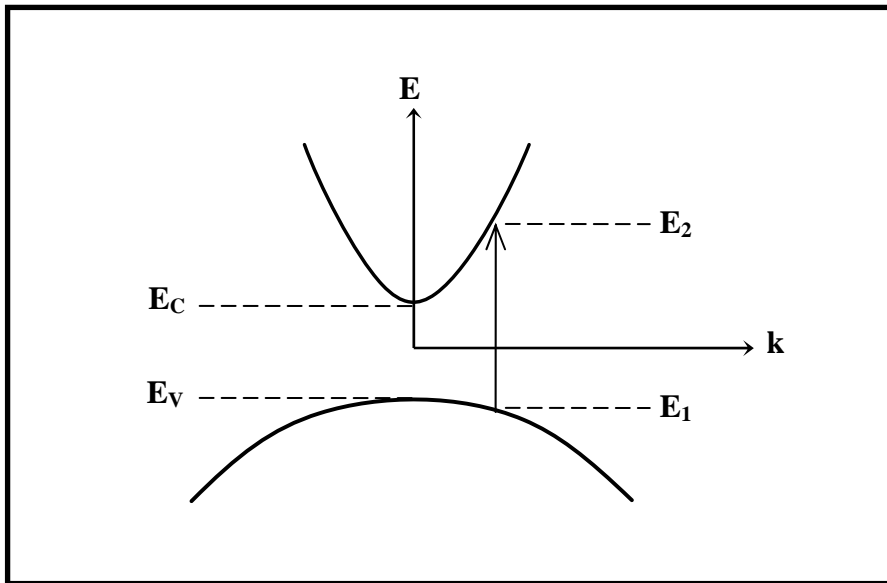
**Fig. 2.2** Electron energy vs. k-vector in semiconductor.
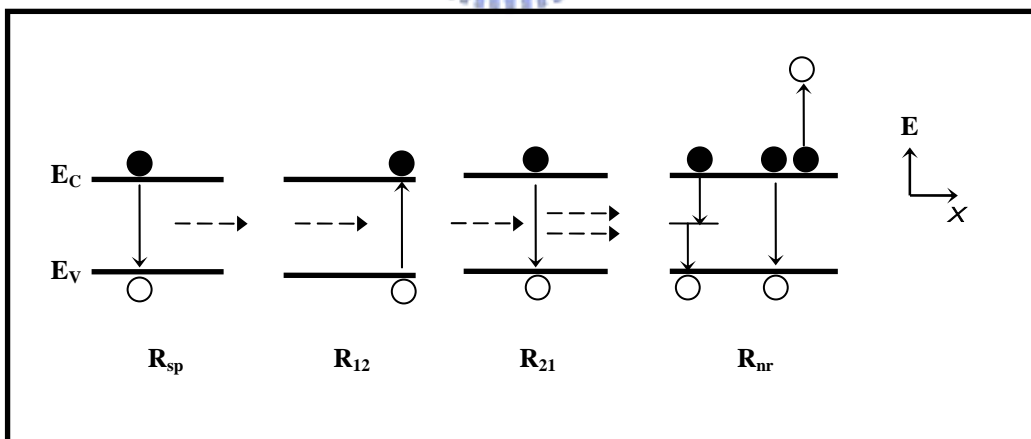


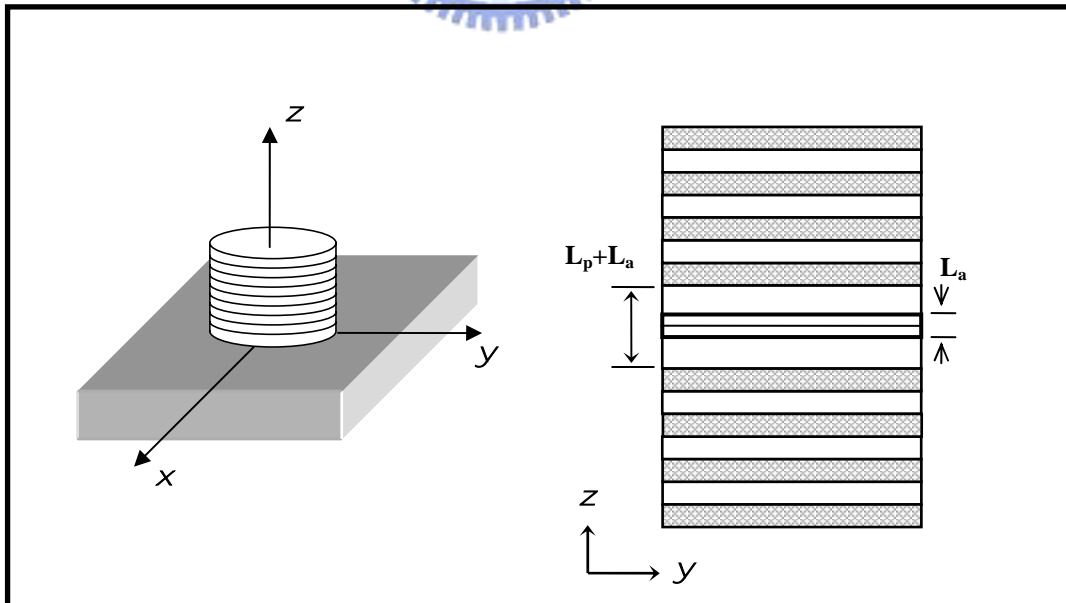**Fig.2.3** Three kinds of electronic transition between conduction and valence bands.

**Fig. 2.4** (a) The schematic of the material structure of the material structure; (b) an energy diagram of the p-i-n structure; (c) refractive index profile; (d) the electric field profile for a mode traveling in the z-direction.
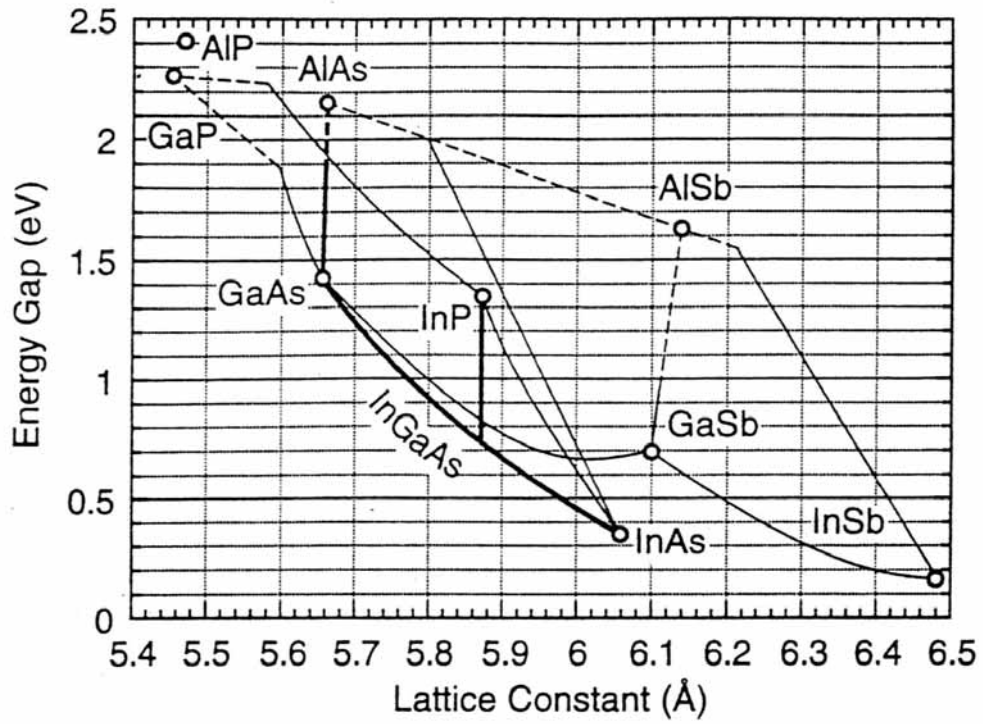
**Fig.2.5** Energy band gap vs. lattice constant of some III-V compound



**Fig. 2.6** General VCSEL scheme

# Chapter 3 Wafer fusion technique

## 3.1 Introduction

Wafer fusion refers to a process by which two mirror-polished wafer adhere to each other without the application of any macroscopic gluing layer or outside force. Wafer fusion is alternatively known as "direct bonding." Although by no means require, in most cases the wafer involved in actual applications are typical semiconductor wafers consisting of single-crystalline materials used in micro- or optoelectronics.

When two atomically smooth and clean surfaces are brought into intimate contact, they adhere to each other via intermolecular forces such as van der Waals forces or hydrogen bonding. By temperature treatment or introducing some monolayers of appropriate molecules into the interlayer, the bonding strength can be increased in such a way that it is comparable with the chemical bond and acts like a welding. Solids of almost any material combination may be joined through this room temperature technique.

The technique of wafer fusion is a viable processing tool to combine semiconductor material independent of their lattice constant. It removes the limitation to lattice matched materials given by epitaxial growth techniques and opens a new degree of freedom for the design of semiconductor device. In contrast to similar techniques, such as epitaxial lift off or silicon/silicon dioxide bonding, wafer fusion does not involve any foreign material at the interface. Instead, both materials are directly joined together and covalent bonds are formed on either side of wafer fused

heterojunctions, which are very similar to those of epitaxially grown interfaces. This enabled the fabrication of novel devices such as the silicon heterointerface photodetector, [3.1, 3.2] wafer fused vertical cavity lasers (VCSELs), [3.3, 3.4] resonant cavity photodetectors, [3.5] or transparent substrate light emitting diodes. [3.6, 3.7]

Wafer fusion has been around for several years and has been applied to a variety of materials. Liau et al. [3.8] were the first to fused III-V base optoelectronic devices to silicon or GaAs substrates, a technique that has been adopted by many groups. [3.9-11] The fusion of InP and GaAs has attracted a lot of interest in the recent year because of its very successful results in the fabrication of long wave length VCSELs [3.12, 3.13]. Wafer fused GaAs / InP VCSELs benefit from the high index contrast and good thermal properties of AlGaAs / GaAs DBR as well as from the high optical quality of InP-based active layers in the 1.3-1.55 μm wavelength regime. Sub-milliampere threshold current and high temperature operation above 100°C have been demonstrated with double fused VCSELs [3.14]. These lasers involve two fused InP / GaAs interfaces inside the optical cavity demonstrating the excellent electrical and optical properties that wafer fusion can be achived.

## 3.2 Intorduction to wafer fusion methods

Several kinds of wafer bonding techniqs have been developed. According to the bonds that formed at adhered interface, we can classify and list as follows.

**(1)** *Bonding by atomic rearrangment* [3.9]

Two wafers were put face to face and a molybdenum block was put on the top of the wafer to assure a close contact of the wafers. The sample was heat to 650°C and held at that temprature for 30min with a hydrogen flow to remove

the native oxide. After the desorbtion of native oxide, surface reconstruction take place on two wafer surfaces to reduce the surface energy. When two surfaces are close enough, new chemical bonds are formed.

**(2) *Van der Waals bonding*** [3.15]

The method utilizes the formation of Van der Waals bond between surface of two wafer to adhere two wafers. Afer clean process, proper thin di-ionized(D.I.) water films was left on two wafers. Two wafers were put face to face and a pressure was applied on the wafers. After all the D.I. water between two wafers disappeared, the two wafers was adhered together.

**(3) *Surface activated bonding*** [3.16]

The surfaces to be bonded are cleaned by sputtering and activated by argon fast atom beam bombardment and then brought into contact with each other in an ultrahigh vacuum at room temperature. The sample was then annealed at low temperature.
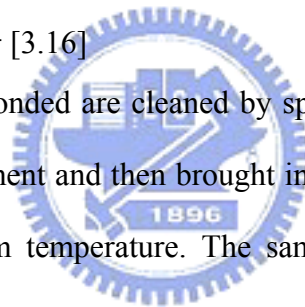
## 3.3 Key issues in the wafer fusion process

One of the common problems associated with wafer fusion is the occurrence of unbonded interface areas which are frequently termed "interface bubbles" or "voids." The unbonded area at the interface will degrate the electrical and optical characterics of devices. The causes of unbonded area include:

**(1) *Smoothness of wafer surface:*** Unsmooth wafer surface will induce the formation of unboned areas causing voids and defects at the fusion interface [3.17].

**(2) *Particles on wafer surface:*** Particles on wafer surface will cause the formation of bubbles or tent-like structure at fusion interace.

**(3) *Uniform pressure:*** During fusion process, pressure is appled on wafers to make the atoms on the wafers surface contact to eachother and form chemical bonds. Ununiform pressure might cause uuniform fused areas or even un-fused areas at the fusion interface.

## 3.4 The wafer fusion system

The main wafer fusion mechanim in this thesis is similar to "bonding by atomic rearrangment." A fixture has been deign which can press the wafers together at elevated temperatures. As illustrated in Fig. 3.1, the fixture consists of two grahpite plates with 18 mm in diameter and two stainless discs with 35 mm in diameter. Three pairs of molybdenum screws and screw nuts are used to fix the whole fixture. Thus, when heated, it can result in a strong compression for the wafer pair loaded inside, due to the large difference in linear thermal expansion of graphite, stainless and molybdenum, which are $9*10^{-6}K^{-1}$, $16*10^{-6}K^{-1}$ and $5.27*10^{-6}K^{-1}$, respectively. The compression can further force the two wafer surface to conform to each other and achieve a very close contact over the entire surface, even though the two original surfaces may have slight bowing or warps. As the two materials contact to each other in pressure and high temperature condition, the chemical bonds form at the interface and the two wafers fused together. Fig.3.2 is the apparatus of the wafer fusion system. The fusion chamber is made by stainless tube, which is located inside the 50cm long furnace. The temperature of the furnace is controlled by the Proportional-Integral-Derivative (PID) controller. The fusion chamber is pumped down and purged with $N_2$.

## 3.5 Experiments for fusion system test

In a long wavelength VCSEL that fabricated with wafer fusion technique, the

two materials bonded together at the interface are typically InP and GaAs. As the whole wafer fusion system was established, we first carried out the fundemental and simply experiments to exame the the fusion system and process.

The wafers used in this work are mirror-polished (100) 0 $^o$ offGaAs and the InP substrates. First the wafers were cleaved into 10*12mm$^2$. The non square geometry was chosen as a means for recognizing the crystallographic orientation of the samples. Then the wafers were cleaned with acetone in ultra-sonic vibrater. After rinsing the wafers in de-ionized water, the mirror-polished surface were brought into contact with the (100) orientation of wafers aligned in de-ionized water and subsequently dried with N$_2$. The sample was put into the fusion fixture depicted in Fig. 3.1. The fixture then was put into the fusion chamber. The fusion process was carried out in the fusion chamber with the furnace temperature at 600$^{\circ}$C in H$_2$ atmosphere for one hour. After fusion process, the two wafers were bonded to each other. The smple were cleaved into pecies to see the cross-section of the fusion interface. We observed that the fused InP and GaAs wafer don't separate after cleave treatmente indicating the well strength existing between the fusion interfaces.

Fig.3.3 and Fig.3.4 show the optical microscope (OM) picture and scanning electron microscope (SEM) image of the cross-section of the cleaved interface respectively. From rudimentary observation of these pictures, the bonding interface is very smooth and there are no interstices at the bonding interface. The stripes on InP side might be caused by the cleavage process when the small different crystallographic orientation between InP and GaAs presented.

For another set of the fused InP / GaAs sample, the electrical contact of Ge/Au/Ni/Au and Ti/Pt/Au   are evaporated by E-gun evaporator on the GaAs and InP side, respectively. After metalization, the sample is annealed at 425°C for 30 seconds by rapid thermal annealing system. Fig. 3.5 shows the I-V curve for fused GaAs/InP sample. The linearity of I-V curve shows that an ideal contact between GaAs and InP interface was obtained with a resistance of 6 ohm for the bonded sample.
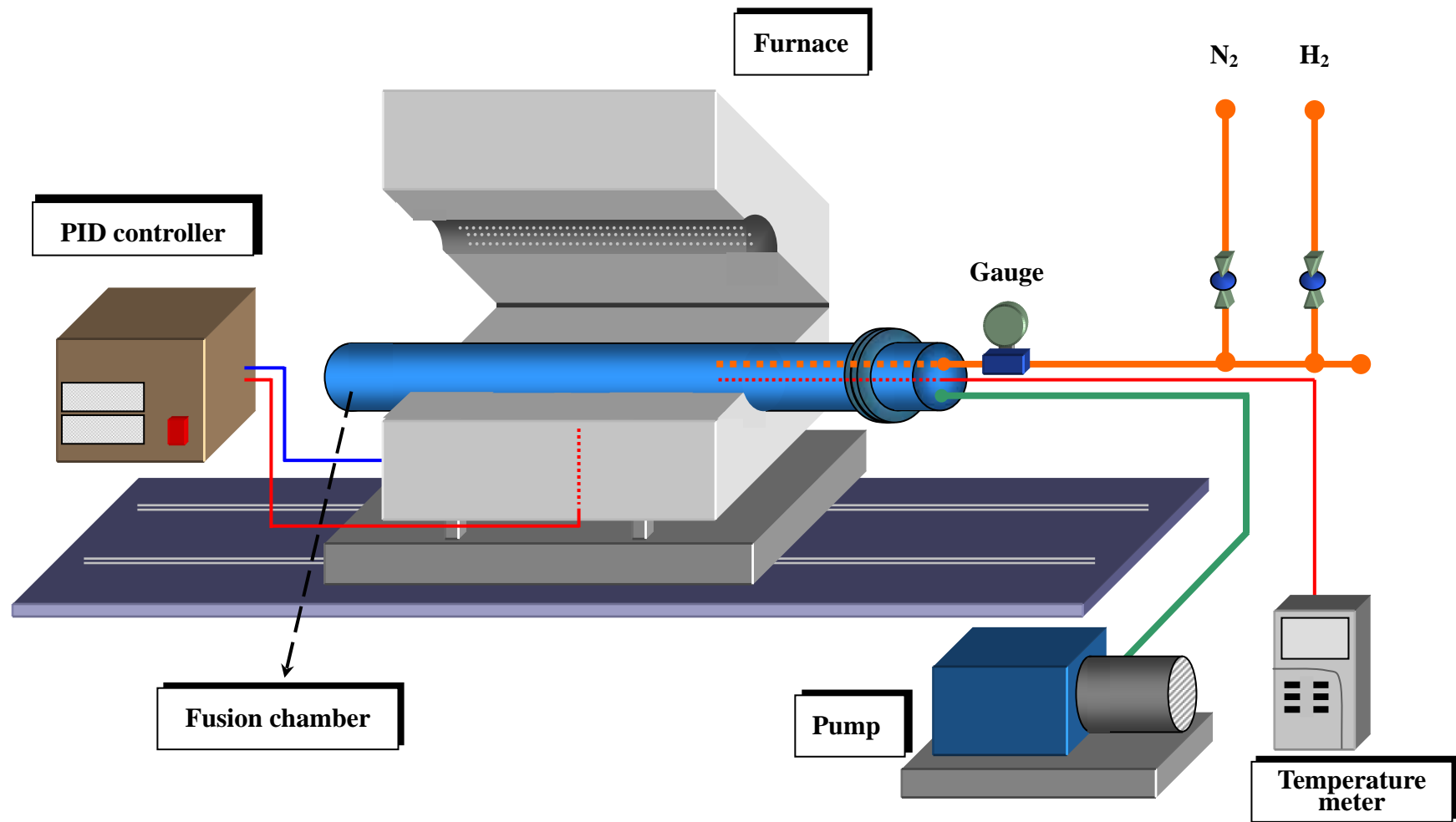
## 3.6 Conclusions

We have established the direct wafer fusion setup and process. Reliable fusion mechanical intensity, smooth fusion interface and good electrical property of fused GaAs/InP have been performed. In the following chapters, further experiments were carried out to examine wafer fusion technique.
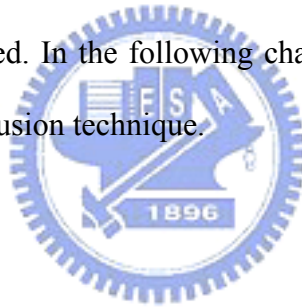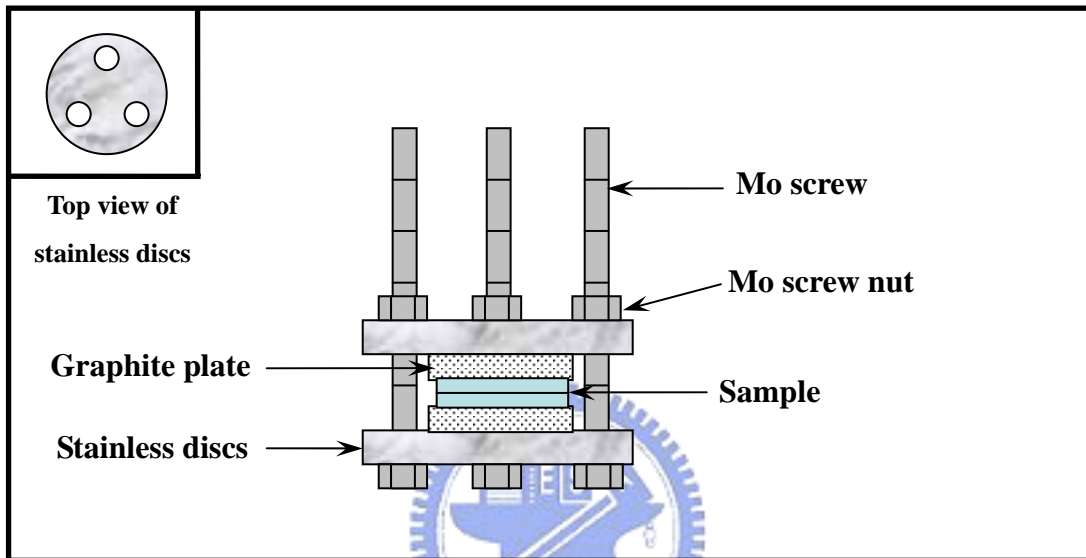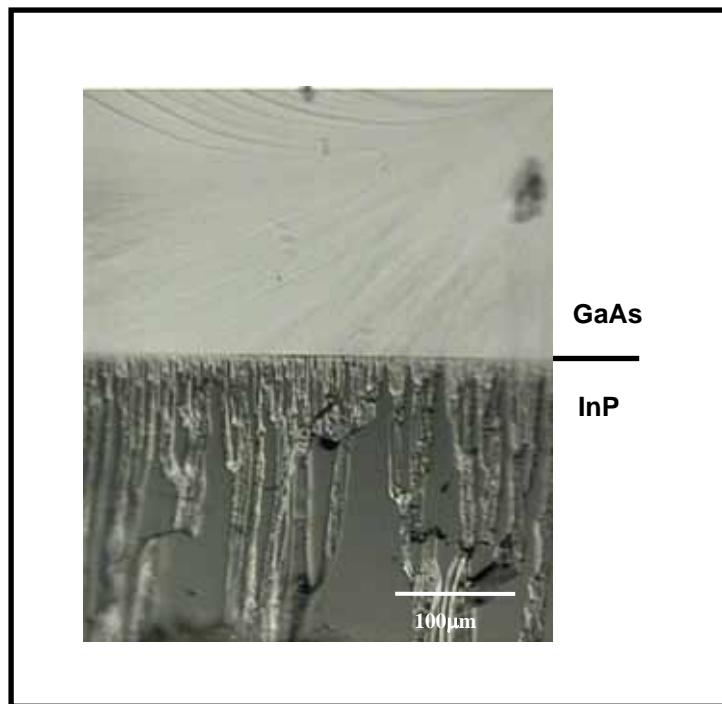
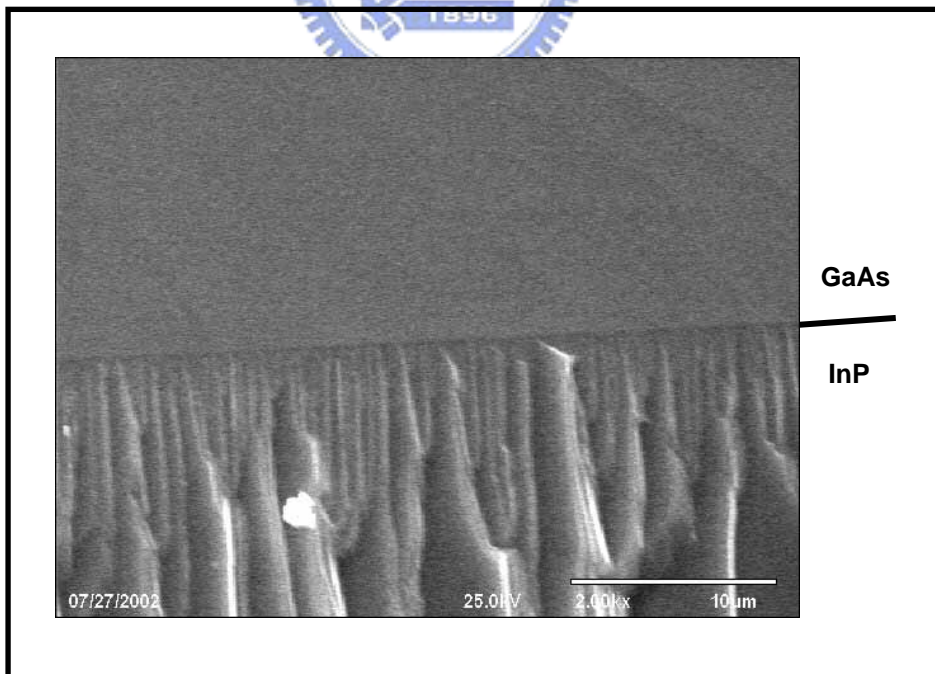**Fig. 3.1** The schematic drawing of the fusion fixture

**Fig.3.2** The apparatus of wafer fusion system

GaAs

InP

100μm

**Fig. 3.3** Optical microscope picture of GaAs/InP interface



GaAs

InP

07/27/2002    25.0kV    2.00kx    10μm

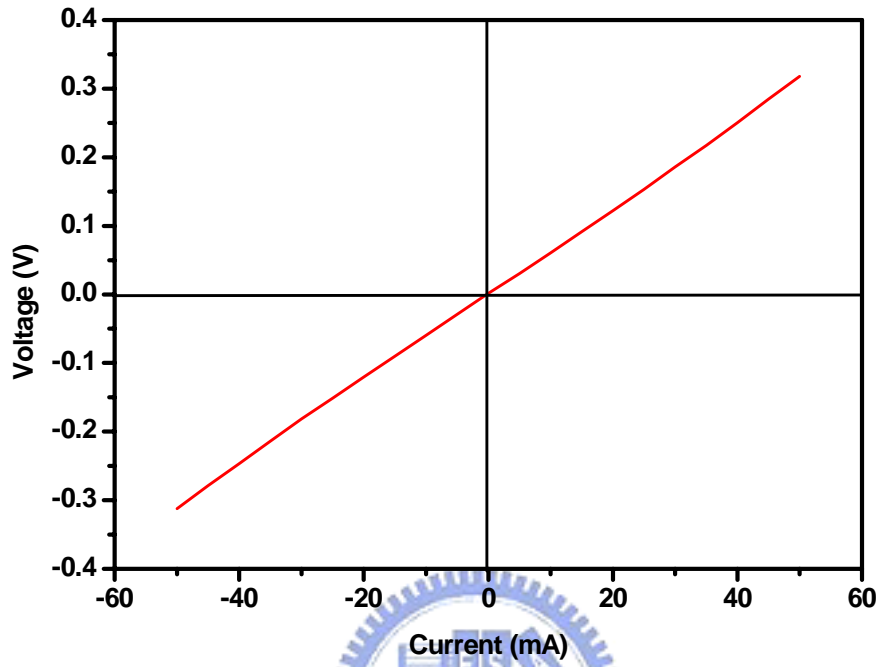**Fig. 3.4** SEM image of GaAs/InP fused interface

**Fig. 3.5** Current-voltage curve for fused InP/GaAs

# Chapter 4 Design rules and simulation of LW-VCSEL with wafer fusion technique

In a VCSEL structure, high reflectivity DBR is a necessary component. In order to minimize the probable optical scattering on the fusion interface, the cavity length and the sequence of DBR materials are concerned issue in designing the structure of the VCSELs fabricated by wafer fusion technique. In this chapter, the reflectance spectra of GaAs/AlAs DBR will be simulated with transfer matrix method. The issues of design and detailed structure of MQW used in this thesis will be discussed. The reflectance spectrum of full VCSEL structure is simulated and compared with the measurement data.

## 4.1 Simulation of DBR reflectance spectra

### 4.1.1 The theory of DBRs

Fig. 4.1 shows a DBR consisting of a stack of quarter-wavelength layers with alternating high and low refractive indices. The reflected waves from each interface will be in phase at the first incident surface and the amplitude of all reflected waves will be added to get high reflectance [4.1].

The principle of DBRs can be numerically calculated by transfer matrix method (TMM).Consider the boundary conditions of the normal incidence of a light wave on a single dielectric layer are shown as in Fig.4.2. In Fig.4.2, the amplitude of the electric vectors of the incident beam, the reflected beam, and the transmitted beam are $E_0$, $E_0'$ and $E_T$, respectively. The electric field amplitudes in the film are $E_1$ and $E_1'$ for the forward and backward traveling waves, respectively.

The boundary conditions require that the electric and magnetic fields be continuous at each interface. These conditions are expressed as follows,

|  | **First Interface** | **Second Interface** |
|---|---|---|
| Electric field | $E_0 + E_0' = E_1 + E_1'$ | $E_1 e^{ikl} + E_1' e^{-ikl} = E_T$ |
| Magnetic field | $H_0 - H_0' = H_1 - H_1'$ **or** $n_0 E_0 - n_0 E_0' = n_1 E_1 - n_1 E_1'$ | $H_1 e^{ikl} + H_1' e^{-ikl} = H_T$ **or** $n_1 E_1 e^{ikl} - n_1 E_1' e^{-ikl} = n_T E_T$ |

Above equations can be simplified as:

$$1 + (E_0'/E_0) = [cos\,kl - i(n_T/n_T)sin\,kl]\,E_T/E_0 \tag{4.1}$$

$$n_0 - n_0(E_0'/E_0) = [-in_1 sin\,kl + n_T cos\,kl]\,E_T/E_0 \tag{4.2}$$

rewrite equations (4.1) and (4.2) in matrix form:

$$\begin{bmatrix} 1 \\ n_0 \end{bmatrix} + \begin{bmatrix} 1 \\ -n_0 \end{bmatrix}(E_0'/E_0) = \begin{bmatrix} cos\,kl & (-i/n_1)sin\,kl \\ -i\,n_1 sin\,kl & cos\,kl \end{bmatrix} \begin{bmatrix} 1 \\ n_T \end{bmatrix}(E_T/E_0) \tag{4.3}$$

Simplify equation (4.3) as:

$$\begin{bmatrix} 1 \\ n_0 \end{bmatrix} + \begin{bmatrix} 1 \\ -n_0 \end{bmatrix} r = M \begin{bmatrix} 1 \\ n_T \end{bmatrix} t \tag{4.4}$$

In multi-layers situation, we can extend equation (4.4) to N layers :

$$\begin{bmatrix} 1 \\ n_0 \end{bmatrix} + \begin{bmatrix} 1 \\ -n_0 \end{bmatrix} r = M_1 M_2 M_3 .... M_N \begin{bmatrix} 1 \\ n_T \end{bmatrix} t = M \begin{bmatrix} 1 \\ n_T \end{bmatrix} t \tag{4.5}$$

Where $M_1$, $M_2$, $M_3$,……$M_N$, are the transfer matrix of each corresponding film.

$$M_1 M_2 M_3 .... M_N = M = \begin{bmatrix} A & B \\ C & D \end{bmatrix} \qquad (4.6)$$

Thus, the reflectance and transmittance of the N layer films are:

$$r = \frac{A n_0 + B n_T n_0 - C - D n_T}{A n_0 + B n_T n_0 + C + D n_T} \qquad (4.7)$$

$$t = \frac{2 n_0}{A n_0 + B n_T n_0 + C + D n_T} \qquad (4.8)$$

### 4.1.2 Simulation of GaAs/AlAs DBRs

With the result as shown in the equation (4.7), the reflectance spectra of the GaAs/AlAs DBR with different number of pairs were simulated with MATLAB 6.0. The centeral wavelength is chosen as 1550nm. The refractive indices of GaAs and AlAs is set as 3.382 and 2.937, respectively. The thickness of GaAs and AlAs are set as in Fig.4.1.

Fig.4.3 shows the reflectance spectra of GaAs/AlAs DBR with different number of pairs. The maximum reflectivity of 10 pairs, 15 pairs and 25 pairs are 96.54%, 99.14%.and 99.95% respectively. The maximum reflectivity is increasing as the number of DBR pairs increased. The stop band of 25 pairs DBR is 140nm.

## 4.2 Simulation and design concern of active regions

### 4.2.1 MQW detailed layer structure and design concern

The detailed layer structure of MQW used in this thesis is shown as Fig.4.3 (a).

Stacks of 290 nm InP / MQW / 290 nm InP / 180 nm InGaAs epitaxy layers were grown by MOCVD on InP substrate. The MQW stands for multi quantum well. The MQW consists of 70nm $In_{0.52}Al_{0.48}As$ / 6 $In_{0.39}Ga_{0.46}Al_{0.15}As$ barriers, 7nm, and 6 $In_{0.73}Ga_{0.2}Al_{0.07}As$ wells, 6nm / $In_{0.52}Al_{0.48}As$, 70nm. The two InP layers serve as cladding layers. InGaAs is the etching stop layer. The total thickness ( $d$ ) of two InP cladding layers and MQW equals to (3/2n) $\lambda$, which determines the optical cavity length of the VCSEL device. The lasing wavelength is therefore determined. The optical cavity length of the VCSEL is typically a single wavelength. In this thesis, the optical cavity length is designed as for special process $-$ wafer fusion process. In the wafer fusion process, as shown in Fig.4.4(b), the two InP cladding layers were fused to the two DBRs. Since the magnitude of the absorption and scattering at fused interfaces is unknown, the standing wave having a null at the fused junctions is a desirable choice. In order to position the null at the fusion interface, the higher refractive index material of DBR must be fused to the InP cladding layer. The cladding layers (InP) have lower refractive indices than the first mirror layer (GaAs) on both sides. For this reason, the interface between these two materials has a negative reflection coefficient when seen from the InP cavity. This means that this reflection adds to the DBR reflectivity, and that in an exactly tuned cavity the standing wave has a null at the fused junction. In the following experiment, it will be shown that the photoluminescence (PL) peak intensity decreases as the distance from the interface decreases. Therefore the cavity length must be chosen as larger than that of the conventional VCSELs structure, in which is chosen as one wavelength. The cavity with thickness of (3/2n) $\lambda$ can provide larger space btween fusion interface and MQWs, to protect MQWs from degrading.

**4.2.2 Simulation of reflectance spectrum of the VCSEL structure**

As mentioned in section 4.2.A, the lasing wavelength is determined by the optical cavity length of the VCSEL structure. In the conventional epitaxil growth process, the optical cavity length can be controlled well. Due to high temperature and high pressure during fusion process, the probable change of thickness of optical cavity and optical property of DBR must be concerned.

A DBR wafer with ( 114.8nm GaAs / 131.5 nm AlAs ) * 25 pairs was fused to a MQW as shown in Fig.4.4a. After fusion, the InP substrate and InGaAs etch stop layer were removed by wet etching followed by coated with 10 pairs of $SiO_2$ / $TiO_2$. The $SiO_2$ / $TiO_2$ dielectric mirror serves as the another mirror of resonant cavity of VCSEL. Fig4.5 shows the final structure of this sample. The measured reflectance spectrum was compared with simulated result which calculated with TFCalc (a program written by Software Spectra Inc of Portland, OR, USA.). Fig.4.6 illustrates the comparison of reflectance spectra between measured and simulated results. Note that the transmission dips of measurement and simulation are equal. It shows that the optical cavity length is the same as we design. It also indicates that the thickness of the cavity ( InP/MQW/InP ) do not alter during wafer fusion process. High reflectivity also shows that the fusion process do not have effect on the optical property of GaAs/AlAs DBR.
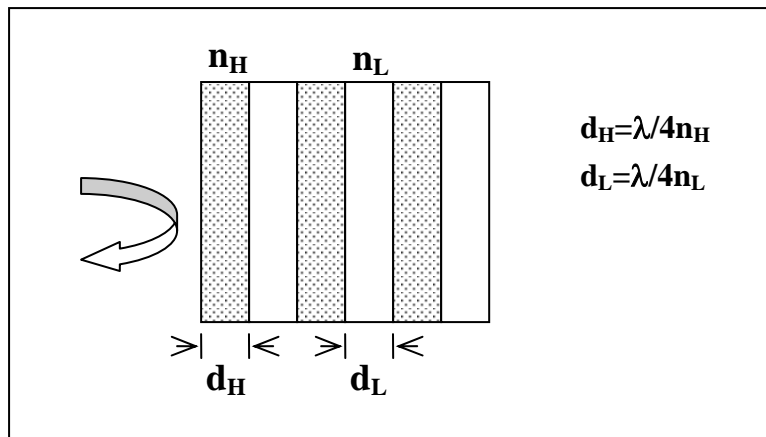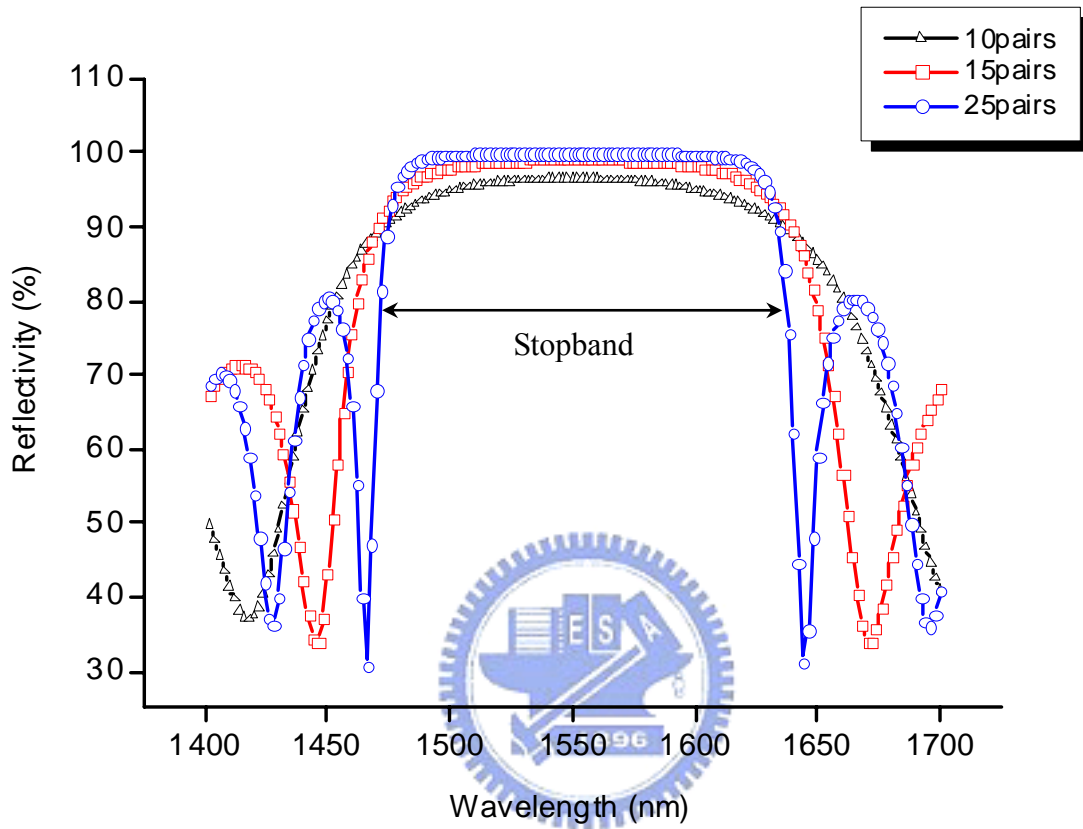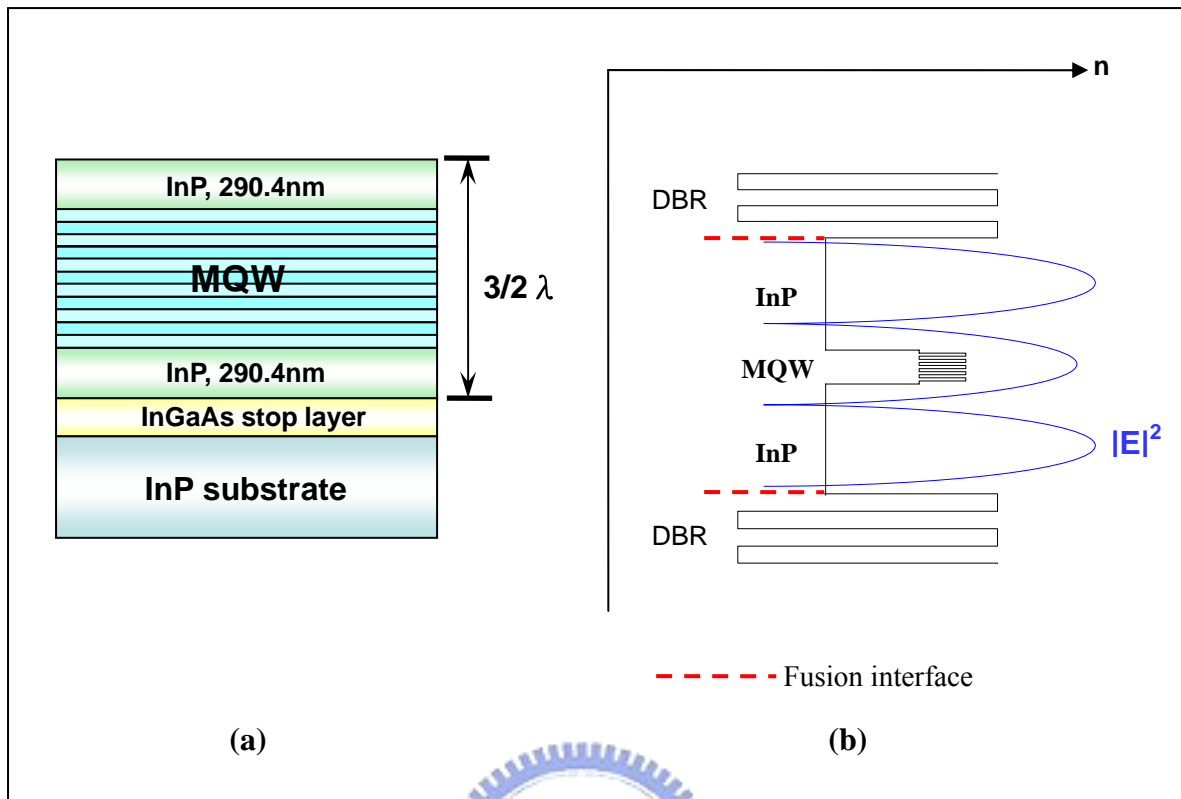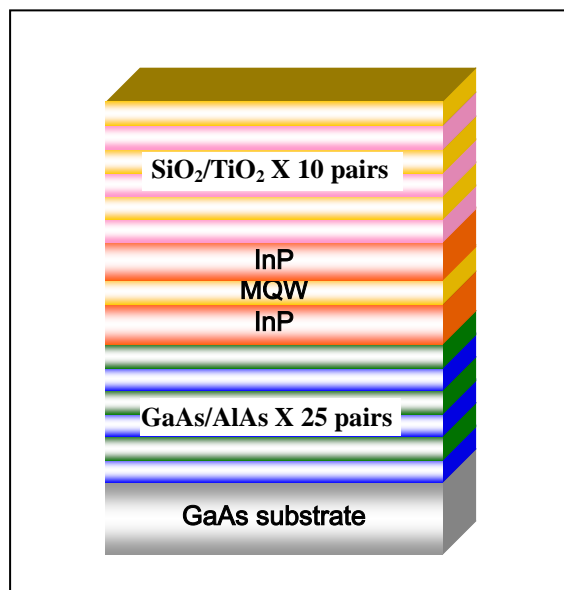
**Fig. 4.1** The schematic of a DBR
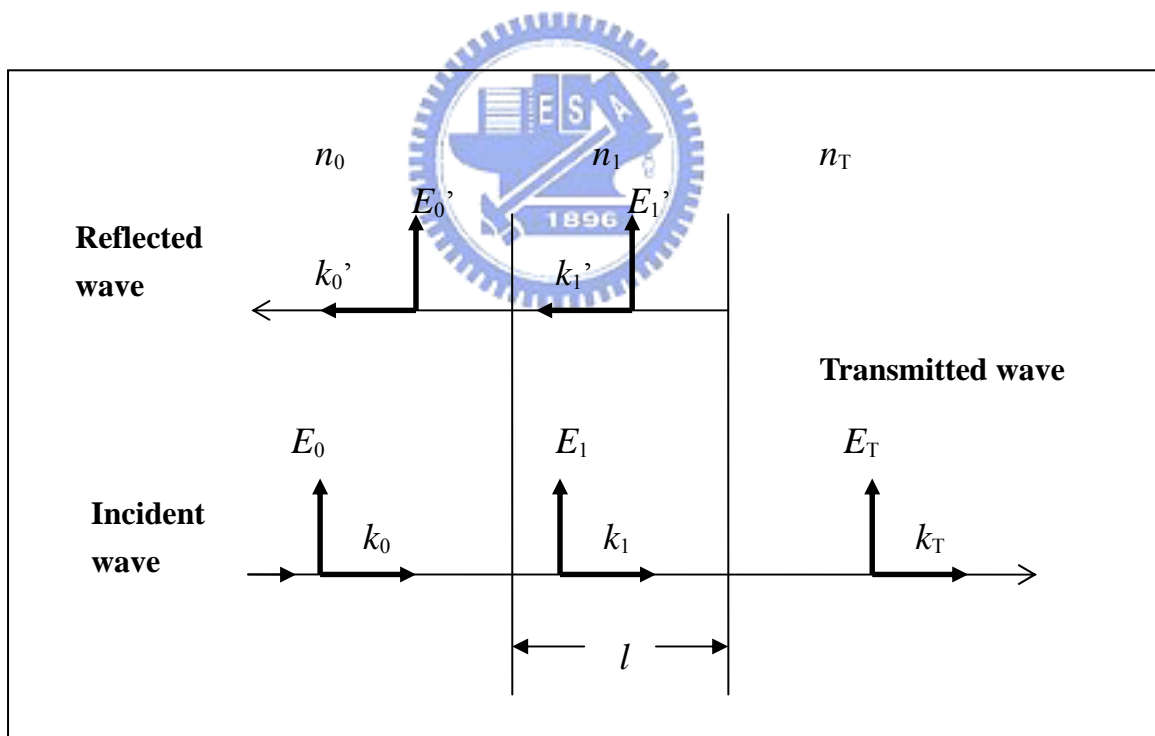


**Fig.4.2** Scheme of wave vector normal incident on single dielectric layer
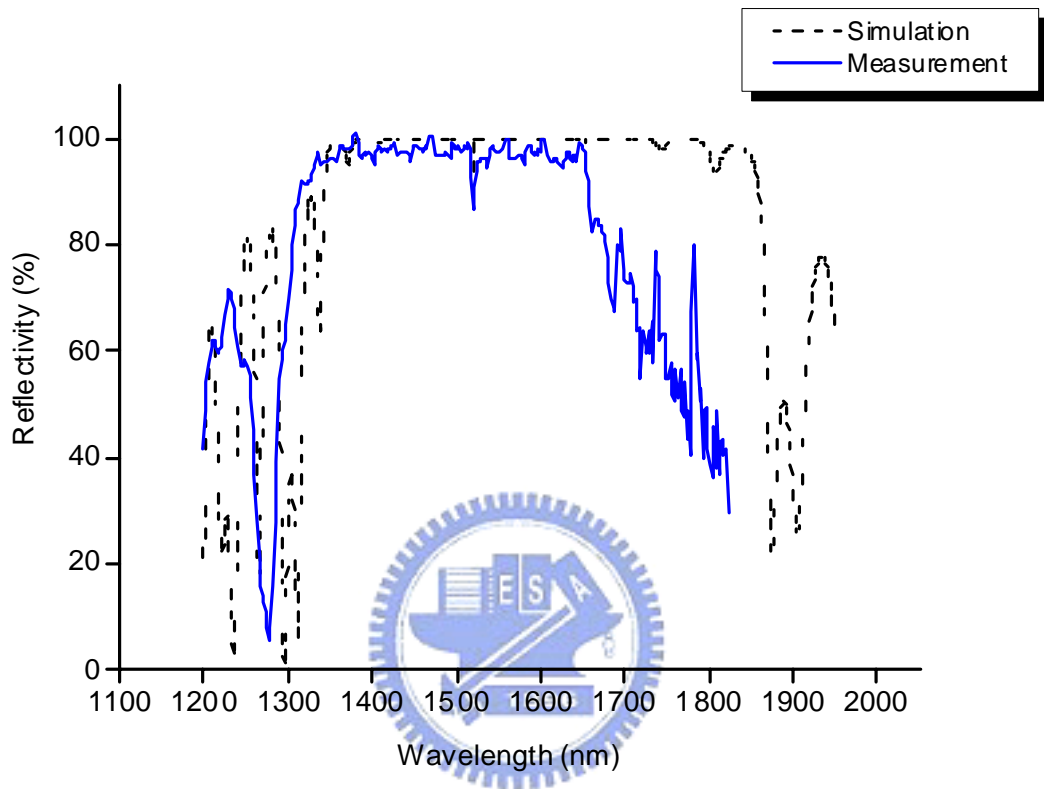
33

**Fig.4.3** The reflectance spectra of GaAs/AlAs DBR with different number of pairs

**Fig.4.4** (a) active region including MQW and InP cladding layers structure details. (b) scheme of standing wave in the resonant cavity



**Fig.4.5** The structure for reflectance spectrum simulation and measurement

**Fig. 4.6** Comparison of reflectance spectrums between measured and simulated results

# Chapter 5 Experimental results and discussions

After initial test experiments for our fusion system and simulation of the full VCSEL structure have been done, in this chapter, we systematically analyzed the influence of fusion process on the performance of VCSELs. First, since the heat produced by the resistance of the operating VCSELs is a considerable issue, the electrical property of the fused junction between n-GaAs and n-InP must be studied. Therefore, the relation between fusion temperature and the resistance of the n-GaAs/n-InP junction has been verified. The optimized fusion temperature for low resistance between n-GaAs/n-InP junction was obtained. As far as the optical properties are concerned, high reflectivity of the DBRs and crystal quality of the MQWs are important issues for the operation of VCSELs. The degradation of the MQW during the fusion process was analyzed. The PL and DBR reflectance spectra after the wafer fusion process were also verified. It was shown that the optical properties of MQWs and DBRs do not degrade after the fusion process. After examined above key points, we demonstrated optically pumped VCSELs which fabricated with wafer fusion technique.

## 5.l Electrical characteristics experiments

The electrical characteristic is a considerable issue of the VCSEL device. Threshold current density, thermal effect, degradation, etc. of a VCSEL relate to the series resistance of itself. In this section, we investigate the basic electrical property for the wafer fused heterojunctions between n-type GaAs and n-type InP layers.

### 5.1.1 Experimental details

A 500nm undoped AlGaAs epitaxial layer was grown by metal organic chemical vapor deposition (MOCVD) at 680°C on Si doped GaAs wafer followed by a 2 μm Si doped GaAs layer. The second sample consisted of a Si doped stack of 300nm InP / 300nm InGaAs / 500nm InP / 320nm InGaAs grown by MOCVD at 620°C on S doped InP wafer (see Fig. 5.1). The InGaAs layer serves as etch stop layer for the substrate removal and fabrication of "fusion trenches" as explained below.

The fusion process was carried out in a stainless steel tube in hydrogen under atmospheric pressure. The fusion temperatures were chosen as 600°C, 450°C and 300°C. Before fusion process, the samples were cleaved into $10*12$ mm$^2$ pieces. The non-square geometry was chosen for recognizing the crystallographic orientation of the samples. The samples were processed with lithography step to pattern an array of trenches (10 μm in width, separated by 2mm) through the InP surface to the first InGaAs etch stop layer. Such trenches have been found to improve the quality of the fused interface by providing gases which were desorbed from samples an effective way to escape [5.2]. After clean step as mentioned in the previous section, the two samples were adhered to each other and were subsequently put into a fixture. The fixture was put into the stainless steel tube and heated to 600°C, 450°C and 300°C respectively for 1 hour in hydrogen atmosphere.

After the fusion process, the InP substrate and the bottom InGaAs etch stop layer was etched off by selective wet chemical etching with HCl : $H_2O$ = 3 : 1 and $H_2SO_4$ : $H_2O_2$ : $H_2O$ = 1 : 1 : 10, respectively. The test structure for I/V analysis consisted of a four-point geometry to exclude the resistance of probes and connecting wire in the measurement system. 200 μm diameter mesas were etched through the InP and

InGaAs layers down to the GaAs substrate, and a pair of concentric ring contacts consisting of electron beam evaporated Ge/Au/Ni/Au for 750/350/200/2000 Å on the top and around the mesa. Then the sample is annealed at 415°C for 30 seconds by rapid thermal annealing system. Fig. 5.2 shows the sample structure and the measurement system setup where $I_D$ is the drive current and $V_M$ is the measured voltage.

### 5.1.2 Results and discussions

Fig. 5.3 shows the I-V characteristics of the fused sample at fusion temperature of 600°C, 450°C and 300°C. The linearity of I-V curves shows that an ideal contact between GaAs and InP interface was obtained. By neglecting the related samll resistance caused by contact metals, contact resistance between semiconductors and metals, InP/InGaAs heterojunction and InP/InGaAs/InP/GaAs layers, the contact resistance can be calculated. The contact resistance were $3.8\,\Omega$-cm$^2$, $4.8\,\Omega$-cm$^2$ and $10\,\Omega$-cm$^2$ for fusion temperature of 300°C, 450°C and 600°C, respectively. It was shown that the sereis resistance is increased as fusion temperature increasing. Accroding to the result published by M.Hammar etl[1]., the resistance is decreased as the fusion teperature increasing. The disagreement might be explained as followed: because there is a little remnant oxygen in the fusion chamber, as the temperature increased, oxide will form on the surfaces of the sample. The quantity of oxide that form on the surface is more at high temperature than that at low temperature. Higher resistance at high fusion temperature cuold due to the more oxide on the surface of sample. 300°C seems to be the best fusion temperature for electrical characteristic between the three fusion temperature.But in  our boservatin, there are some striped areas of InP/InGaAs/InP layers after the InP substrate was removed. Low temperature may not provide enough pressure and thermal energy to fuse the materialas together.

Hence, 450°C is suggested to be the proper fusion temperature for good fusion interface and lower resistance.

## 5.2 Optical characteristics experiments

The optical characteristic is a key issue whenever the performance of a VCSEL is discussed. As mentioned in chapter 2, high reflectivity DBR and high gain active region are important for LW-VCSEL. In this section, we first find the influence of the distance between fusion interface and active region on active region photoluminescence (PL) intensity. Second, we compare the PL signal of the InGaAlAs MQW before and after fusion process. The reflectivity of DBR before and after fusion process is also compared. Finally, we demonstrate a VCSEL structure with bouble fused DBRs for optical pumping.

### 5.2.1 The influence of distance between fusion interface and active region on active region PL intensity

#### 5.2.1.A   Experimental details

Stacks of 290 nm InP / MQW / 290 nm InP / 180 nm InGaAs epitaxial layers were grown by MOCVD on InP substrate. The MQW stands for multi quantum well. The MQW consists of 70nm $In_{0.52}Al_{0.48}As$ / 6 $In_{0.39}Ga_{0.46}Al_{0.15}As$ barriers, 7nm, and 6 $In_{0.73}Ga_{0.2}Al_{0.07}As$ wells, 6nm / $In_{0.52}Al_{0.48}As$, 70nm. The two InP layers serve as cladding layers. InGaAs is the etching stop layer. Another wafer was grown with 25 pairs of GaAs/AlAs on a GaAs substrate.

Before the fusion process, the samples were cleaved into four pieces with dimension of 10*12 mm$^2$. Three of these four samples were subsequently wet etched

to change the thickness of the top InP layers. The top InP layers of these four samples are 290nm, 190nm, 140nm and 90nm. These four samples were fused with GaAs wafers with dimension of 10*12 mm$^2$ at 600°C for 1 hour in hydrogen atmosphere. After fusion, the InP substrates and InGaAs stop layers were selective wet chemical etched with HCl : H$_2$O = 3 : 1 and H$_2$SO$_4$ : H$_2$O$_2$ : H$_2$O = 1 : 1 : 10. The PL was measured using 532nm laser with power of 4.4mW. The process flowchart was shown in Fig. 5.4.

### 5.2.1.B    Results and discussions

Fig. 5.5 shows the PL spectra of these four samples. Dependence of the PL peak intensity on the distance from the fusion interface is shown as Fig. 5.6. The PL peak intensity decreases as the distance from the interface decreases. It has been shown by Ram et al.[6] that all dislocations occurring during fusion are localized to within 200 nm from the fused junction. The migrating dislocation might degrade the crystal quality and decrease the PL peak intensity. The dislocations that migrate to MQW increase as the distance from the interface decrease. In the meanwhile, PL peak intensity decrease. With this conclusion, we should take the distance between fusion interface and active region into consideration when we design the VCSEL structure.


## 5.2.2 Comparisons of PL/ DBR reflectance spectra before and after wafer fusion process


### 5.2.2.A Experimental details

Stacks of 290 nm InP / MQW / 290 nm InP / 180 nm InGaAs epitaxial layers were grown by MOCVD on InP substrate. The MQW stands for multi quantum well. The MQW consists of 70nm In$_{0.52}$Al$_{0.48}$As / 6 In$_{0.39}$Ga$_{0.46}$Al$_{0.15}$As barriers, 7nm, and 6 In$_{0.73}$Ga$_{0.2}$Al$_{0.07}$As wells, 6nm / In$_{0.52}$Al$_{0.48}$As, 70nm. The two InP layers serve as

cladding layers. InGaAs is the etching stop layer. Another wafer is the DBR consisting of a stack of (114.8nm GaAs / 131.5 nm AlAs) * 25 pairs grown on GaAs wafer by MOCVD.

Before the fusion process, the MQW and DBR wafers were cleaved into 10*12 mm$^2$ pieces. The PL of one MQW sample was measured using 532nm laser with 4.4mW. The reflectivity of one DBR sample was also measured. After the fusion process with the MQW and DBR samples at 600°C in hydrogen atmosphere, the InP substrate and InGaAs etch stop layer were removed by wet etching. The process flowchat was shown as Fig.5.7.

### 5.2.2.B Results and discussions

Fig. 5.8 shows the PL spectra of the sample before and after the wafer fusion. Due to the high reflectivity of the DBR, the PL peak intensity of the sample after fusion is 4.4 times higher than that before fusion process. The peak wavelength of MQW retained at 1521nm after fusion process. The full width at half of maximun (FWHM) of sample after fusion is 29 nm which is narrower than that (63 nm) of sample before fusion. An optical resonant cavity was formed after the fusion, which modified the peak wavelength and shrink the PL FWHM.

The DBR reflectivity spectra before and after fusion process are shown as    Fig. 5.9. The stop-band width of the DBR is the same value before and after the fusion process. Limited by measurement instrument, we can only get relative reflective spectrum of the DBR. For this reason, exact maximum reflectivity of DBR is not available. Nevertheless, the maximum reflectivity of DBR after fusion can be calculated according to the following experimental result. The maximum reflectivity

of DBR is higher than 95%. As mentioned before, band width and maximum reflectivity of DBR are very important for VCSEL device. It was confirmed that the fusion process does not affect these two key characteristics of DBR.

## 5.3 Optical pumping of the VCSEL structure

In this section, the VCSEL structure consisting of a fused bottom DBR with the MQW and a deposited dielectric top DBR was demonstrated. Next, the another VCSEL structure consisting of the top and bottom fused DBRs with the MQW was also demonstrated.

### 5.3.1 The VCSEL structure with one fused DBR with one dielectric mirror

The full VCSEL structure shown in Fig.5.10 consists of one fused DBR and MQW followed by 10 pairs of $SiO_2$ / $TiO_2$ serving as another mirror of the resonant cavity. The sample was optically pumped using a mode-locked Ti:sapphire laser. The wavelength of the pumping laser was tuned at 900nm with 0.2 pico second pulses and a repetition rate of 76 MHz, although the pumping wavelength at slightly beyond 1.1μm would be more desirable to avoid absorption of the InP ($\lambda_g$ = 0.9μm) spacer layer and InGaAlAs ($\lambda_g$ = 1.1μm) cladding layer. The spot diameter of the pumping beam on the top dielectric mirror is estimated to be 100 μm. The device was pumped through the $SiO_2$ / $TiO_2$ dielectric mirror side. Detailed setups of the optical pumping system are shown as Fig. 5.11.

Fig. 5.12 shows the spectra versus different pumping powers. The minimum line width of the spectra is limited by the TRIAX to be about 1 nm, therefore the lasing operation can't be easily judged by the spectrum line width. Pumping power versus peak intensity (L-L) curve is shown as Fig.5.13. When pumping power is less than

400mW, the wavelength of peak intensity is blue shifted from 1626.6 nm at 100 mW to 1623.5 nm at 400 mW. When pumping power is lager than 400 mW, the wavelength of peak intensity is nearly unchanged. In theory, the emission wavelength will pin after the threshold condition is reached. On the other hand, the band filling effect could be responsible for the blue-shift emission wavelength before the threshold condition. We can also conclude that the threshold pumping power is 350 mW from the L-L curve shown in Fig.5.13. The equivalent threshold current density is calculated to be 3 kA/cm$^2$. The relatively large threshold current density might due to the non-optimized quantum well structure. In addition, the absorption of the pumping light in the cladding layers and the reflection at the surface might be responsible for high threshold current density.

### 5.3.2 The VCSEL structure with double fused DBRs

The fusion process flow chart of double fused VCSEL structure is shown in Fig.5.14. The bottom mirror is a 30-period GaAs/AlAs mirror. The active region consists of three sets of five InGaAlAs quantum wells and barriers. The three sets of MQW are located at where the antinodes of standing wave pattern locate in the resonant cavity. Before fusion the MQW and DBR wafers were cleaved into 10*12 mm$^2$ pieces. After pre-fusion process as mentioned in the previous section, the MQW and bottom DBR wafers was fused at 600°C in hydrogen at 1atm. After first fusion process, the InP substrate and InGaAs etch stop layer were removed by wet etching. In the second fusion process, the fused sample was fused with another 25-period GaAs/AlAs top DBR with a 30nm InGaP stop layer. Then the GaAs substrate and the InGaP stop layer were removed by wet etching sequently. The process flowchat was shown as Fig.5.14. The SEM image of the final double fusion VCSEL structure was shown as Fig.5.15. The well fused interfaces were obtained.

The final double fused VCSEL was placed in the optical pumping system. The conditions of Ti:sapphire laser are the same as mentioned in section 5.3.1. Fig.5.16 shows pumping result of the VCSEL. The threshold pumping power density is 5 kW/cm$^2$ at room temperature. The inset shows the VCSEL emission spectrum at the pumping power density of 8 kW/cm$^2$. Peak emission wavelength is 1527 nm and the FWHM is 1.8nm. The equivalent threshold current density is calculated to be 4 kA/cm$^2$. Due to Auger recombination of InP system material [5.3], the threshold current density is higher than that of single fused DBR / dielectric DBR. Take the Auger recombination into considerations, MQW with more pairs has lower material gain above certain injection current density (depend on materials and structure of MQW).
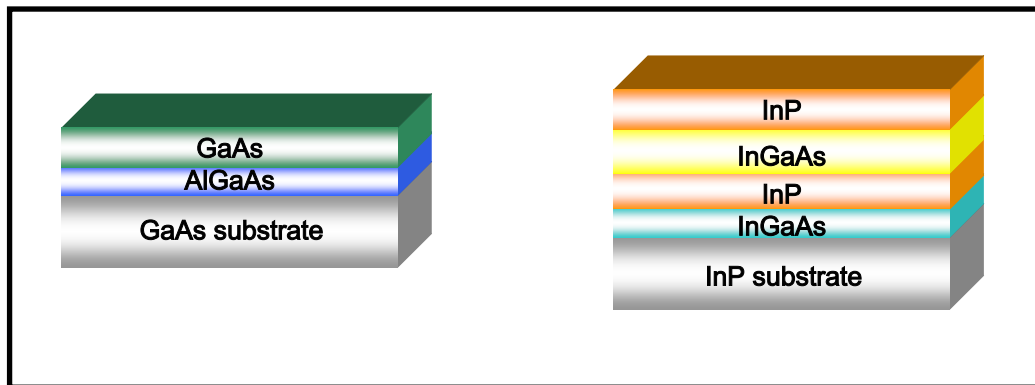
**Fig. 5.1** The layer structure of GaAs and InP
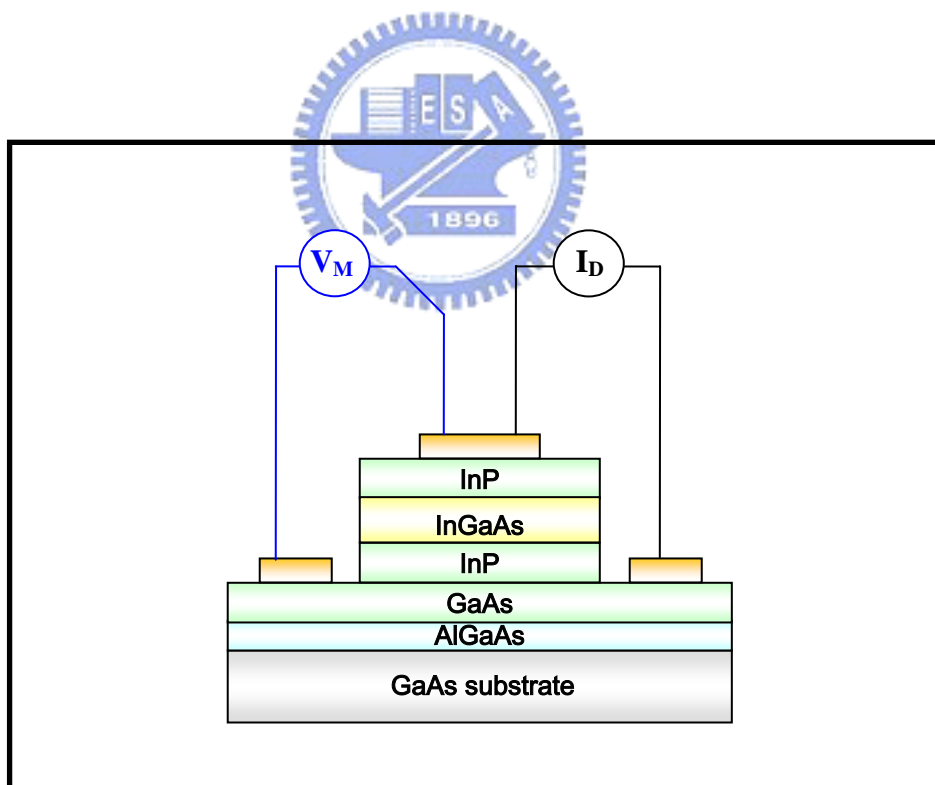


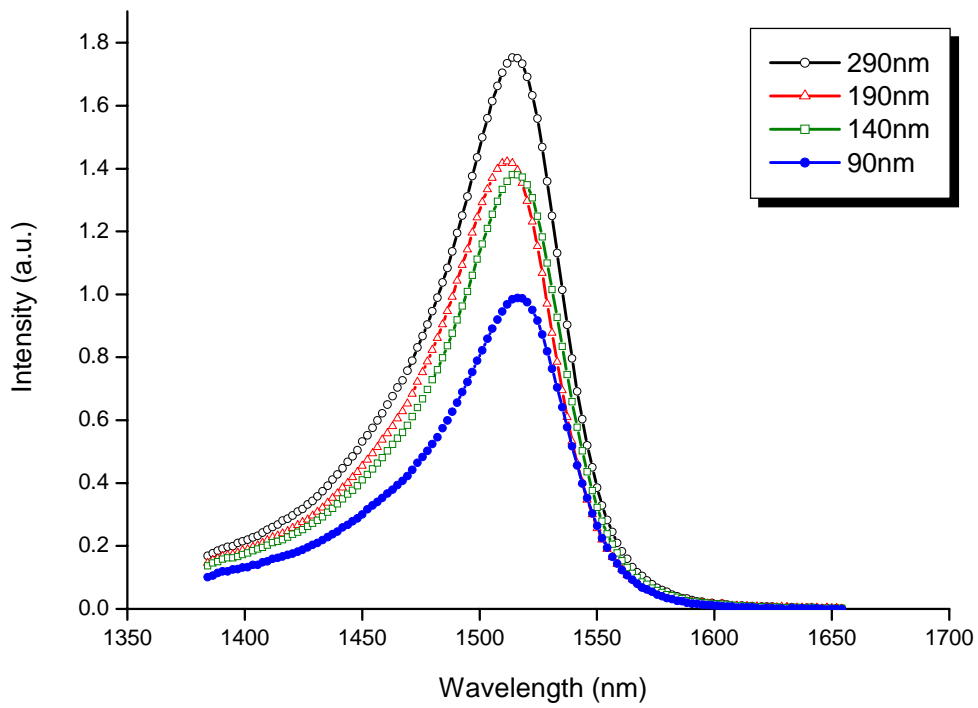**Fig. 5.2** Sample structure for electrical measurement and
measurement scheme
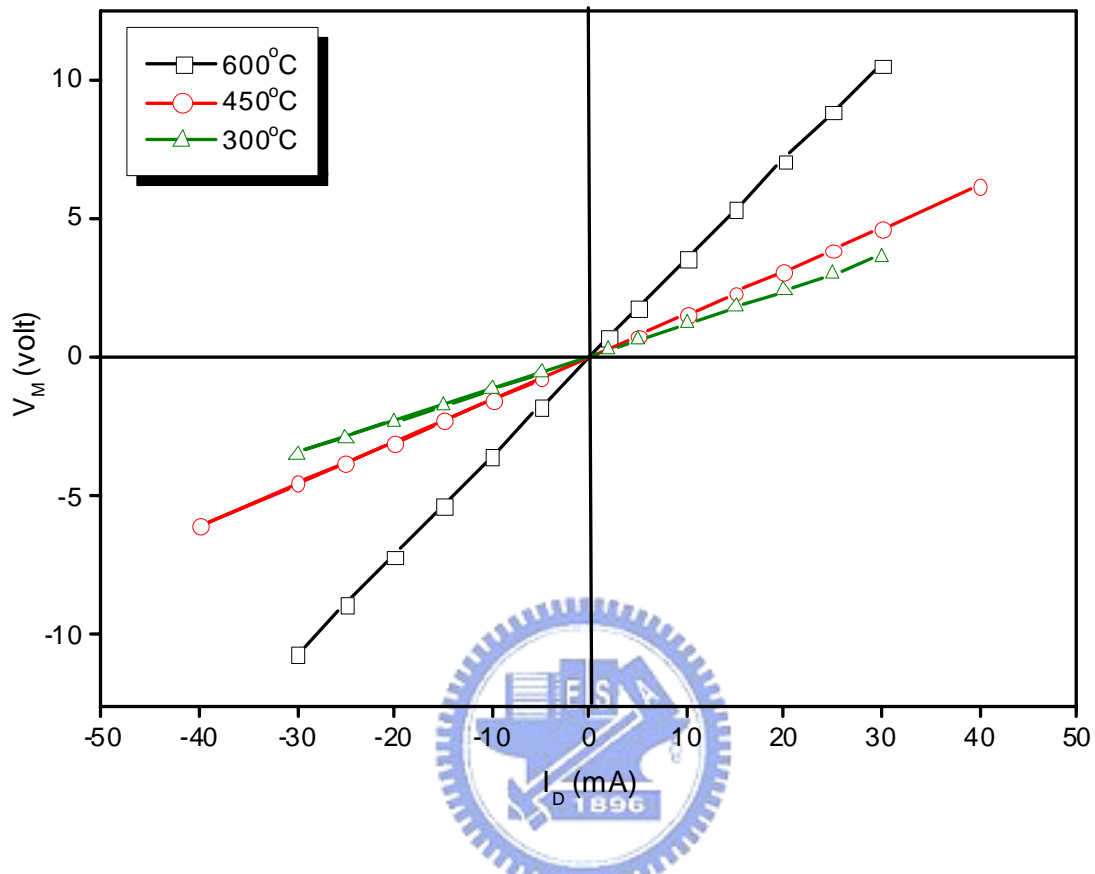
**Fig. 5.3** I-V curve with three different fusion teperatures
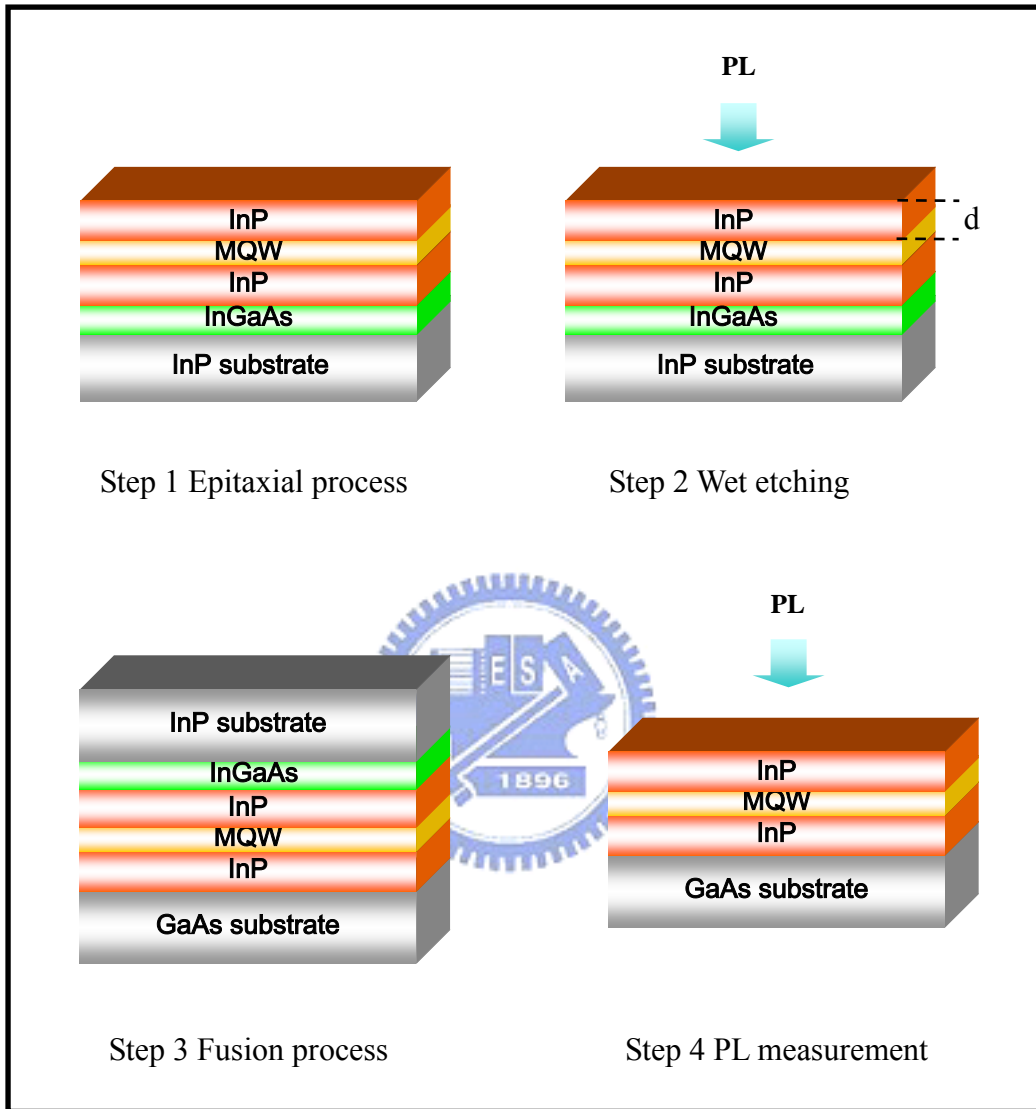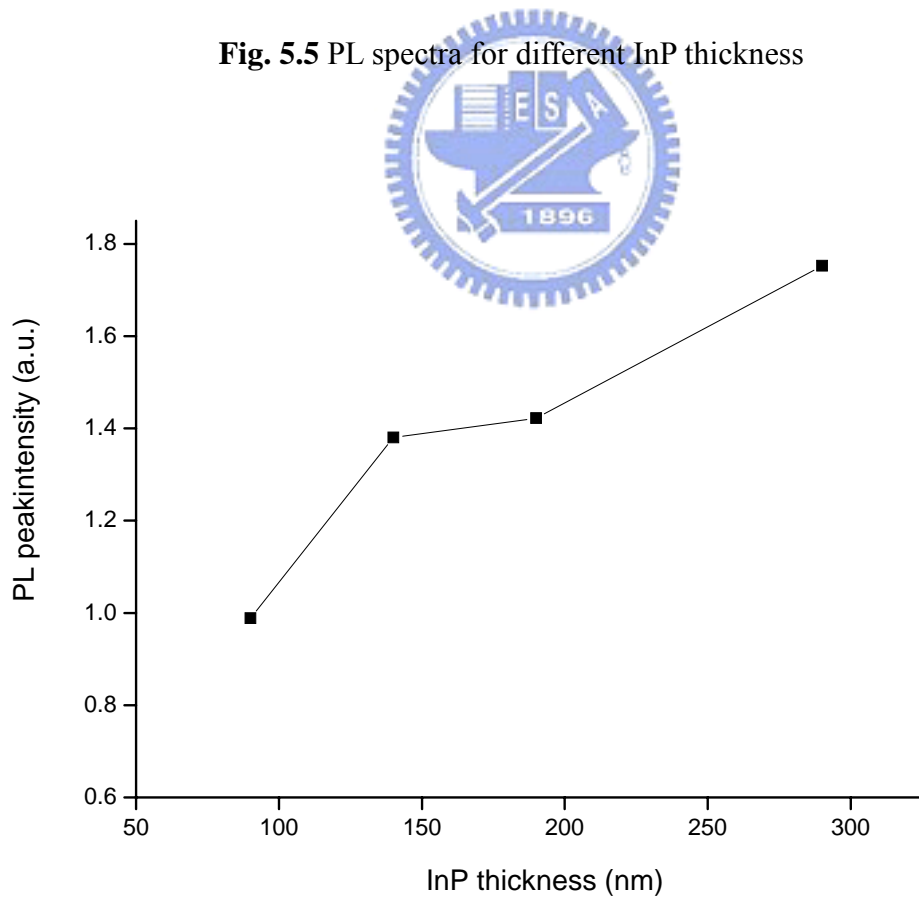
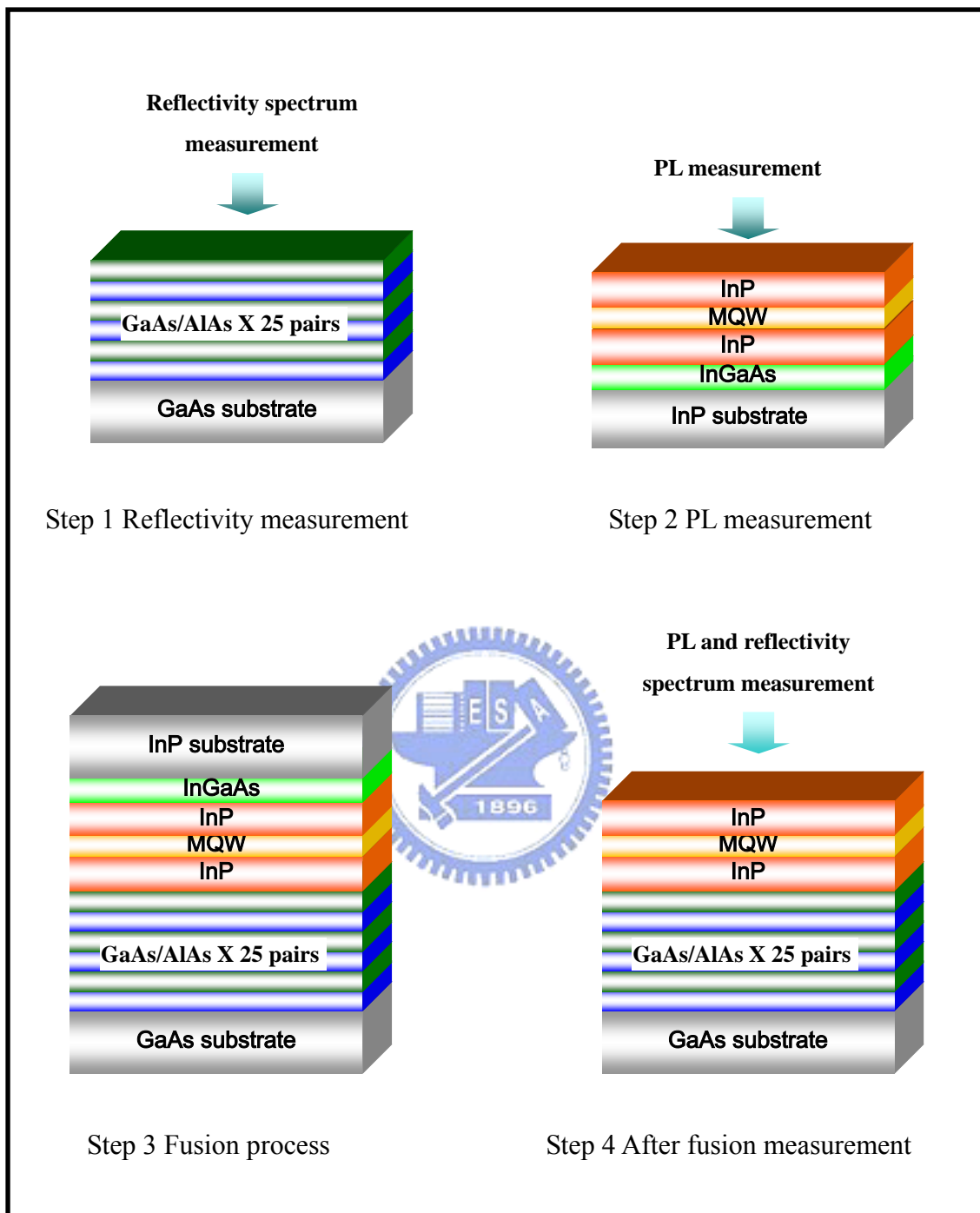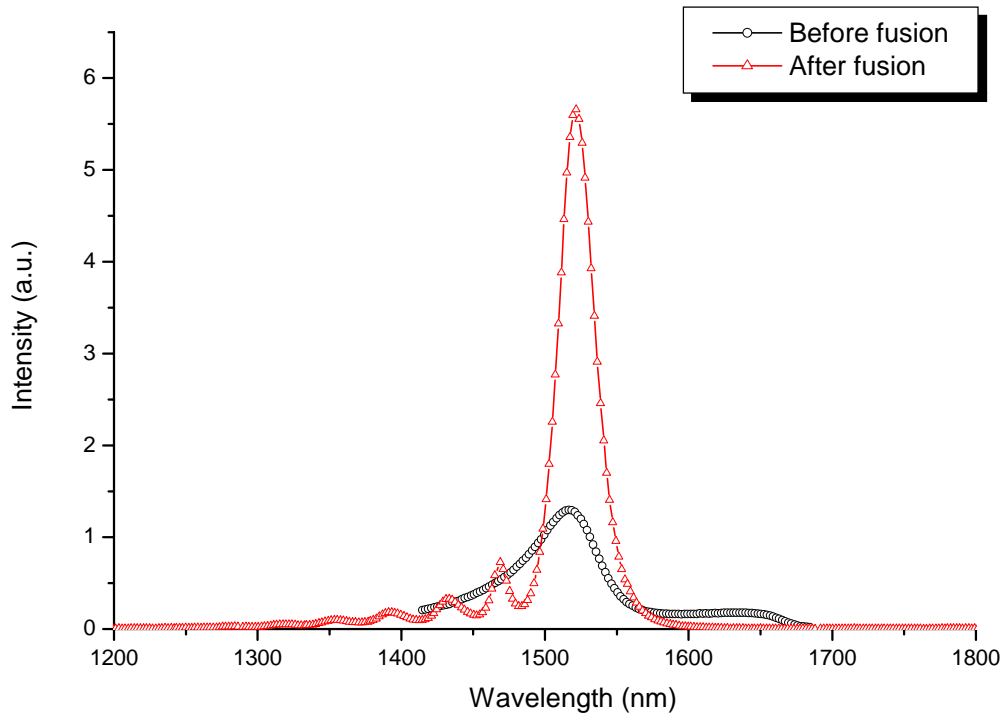**Fig. 5.4** Process for MQW quality experiment

**Fig. 5.5** PL spectra for different InP thickness



**Fig. 5.6** Dependence of the PL peak intensity on the
distance from the fusion interface

**Reflectivity spectrum**

**measurement**

GaAs/AlAs X 25 pairs

GaAs substrate

Step 1 Reflectivity measurement

**PL measurement**

InP

MQW

InP

InGaAs

InP substrate

Step 2 PL measurement

InP substrate

InGaAs

InP

MQW

InP

GaAs/AlAs X 25 pairs

GaAs substrate

Step 3 Fusion process

**PL and reflectivity**

**spectrum measurement**

InP

MQW

InP

GaAs/AlAs X 25 pairs
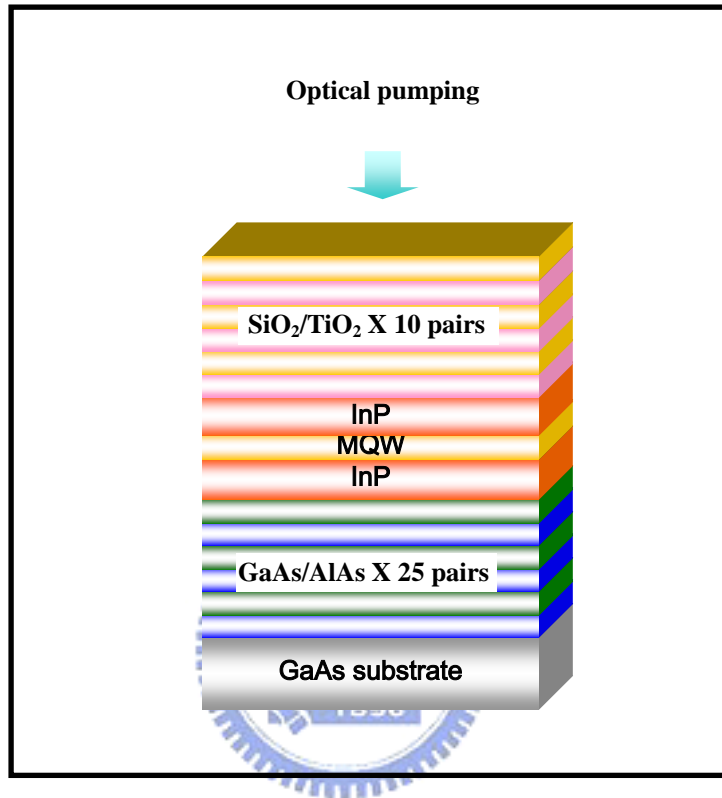
GaAs substrate

Step 4 After fusion measurement

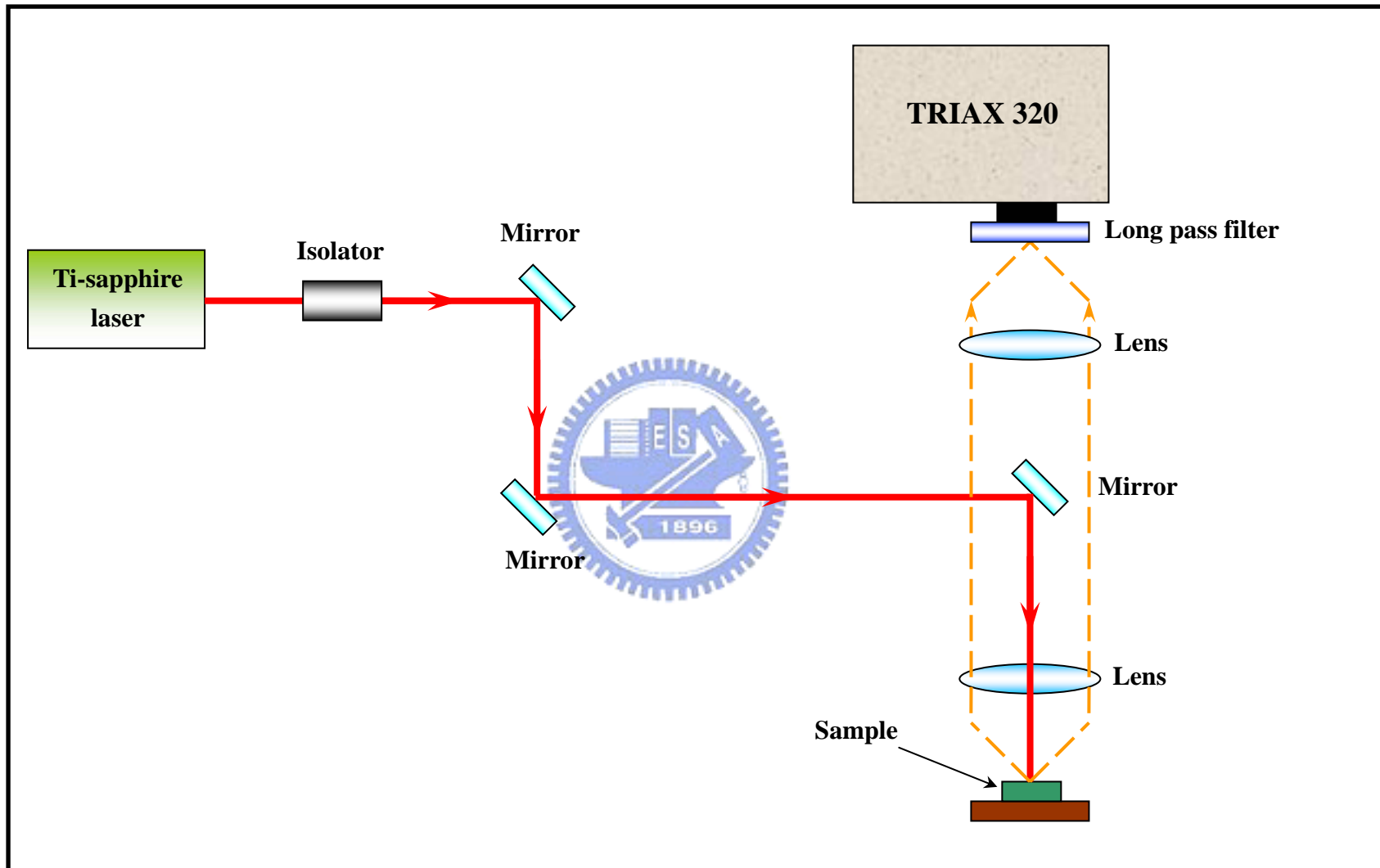**Fig.5.7** Flowchart of MQW/DBR fusion process

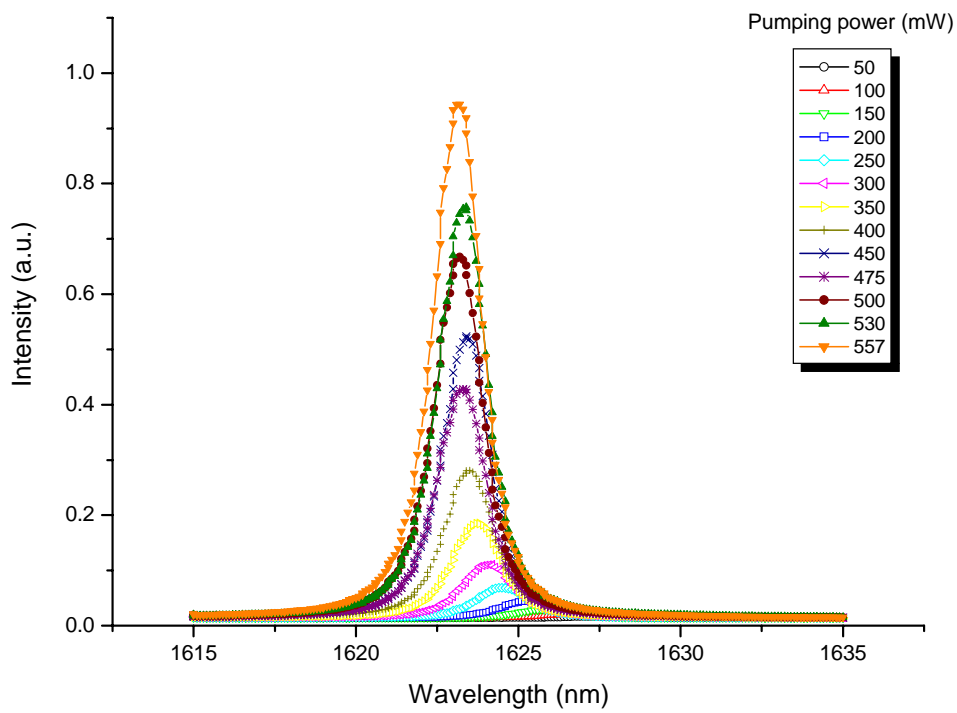**Fig. 5.8** PL spectra of MQW before and after wafer fusion
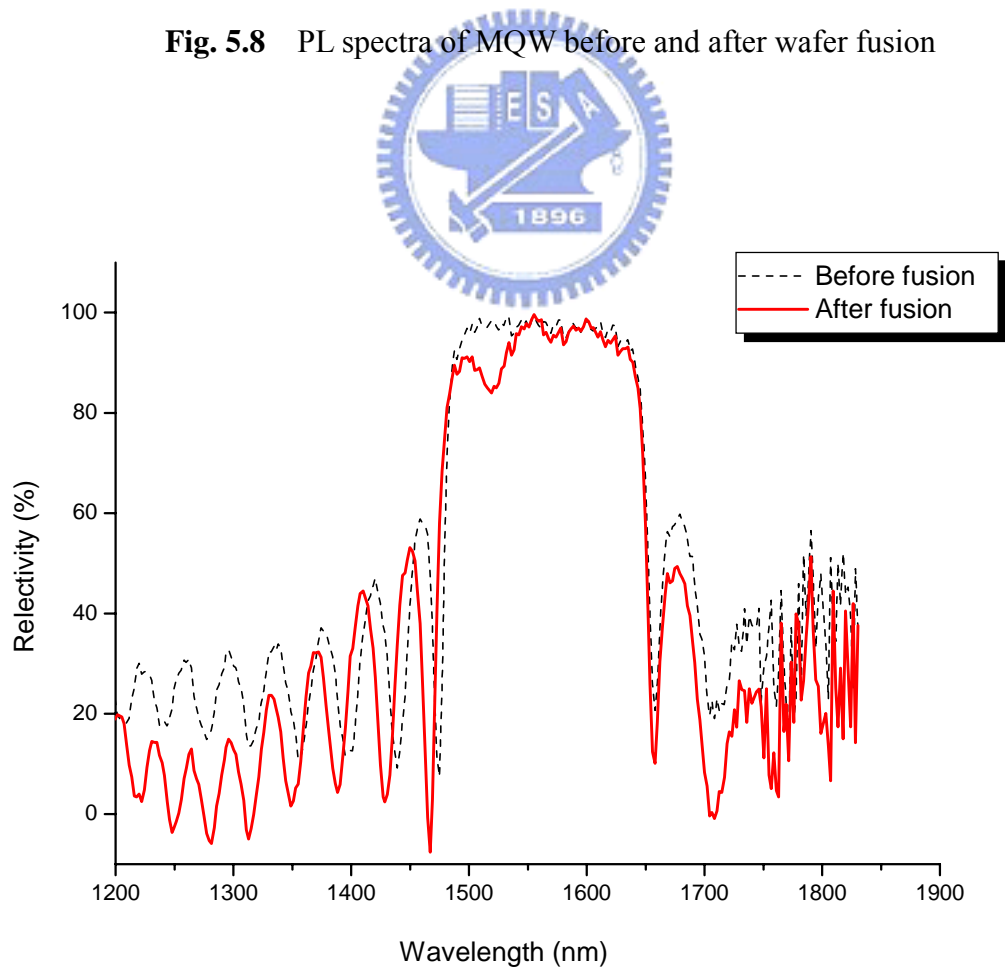


**Fig. 5.9** The DBR reflectivity spectra before and after fusion
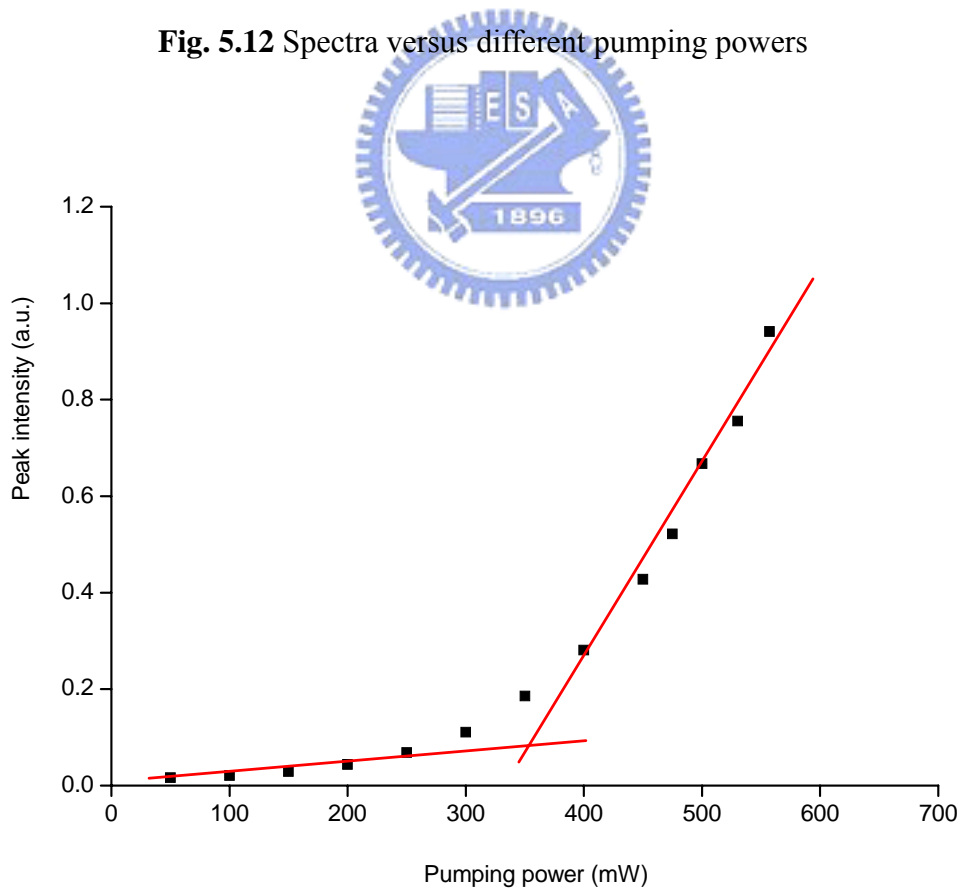
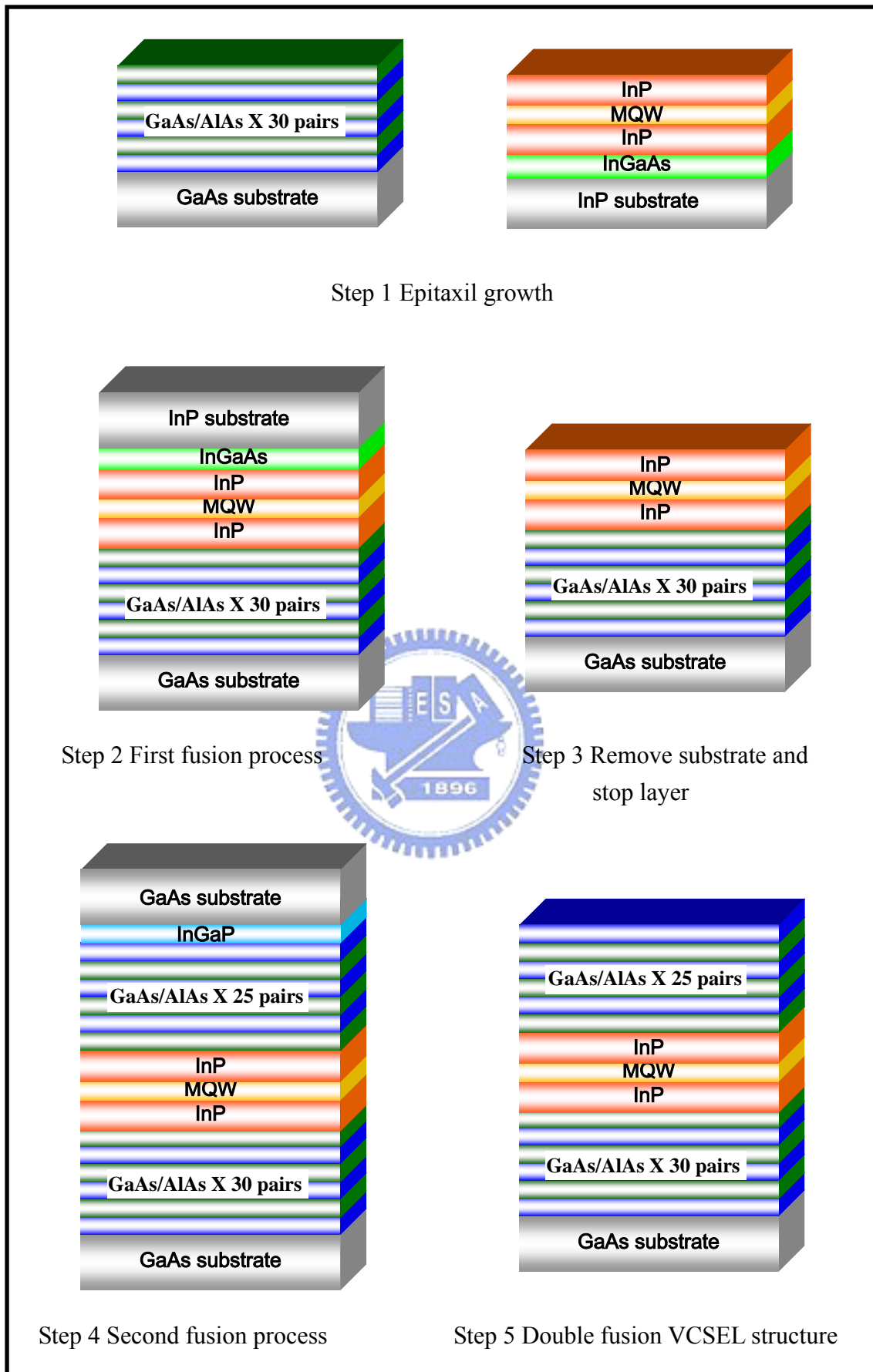**Fig. 5.10** VCSE structure for optical pumping

**Fig. 5.11** Scheme of optical pumping / PL

**Fig. 5.12** Spectra versus different pumping powers



**Fig.5.13** L-I curve of optical pumping

Step 1 Epitaxil growth

Step 2 First fusion process

Step 3 Remove substrate and stop layer

Step 4 Second fusion process

Step 5 Double fusion VCSEL structure
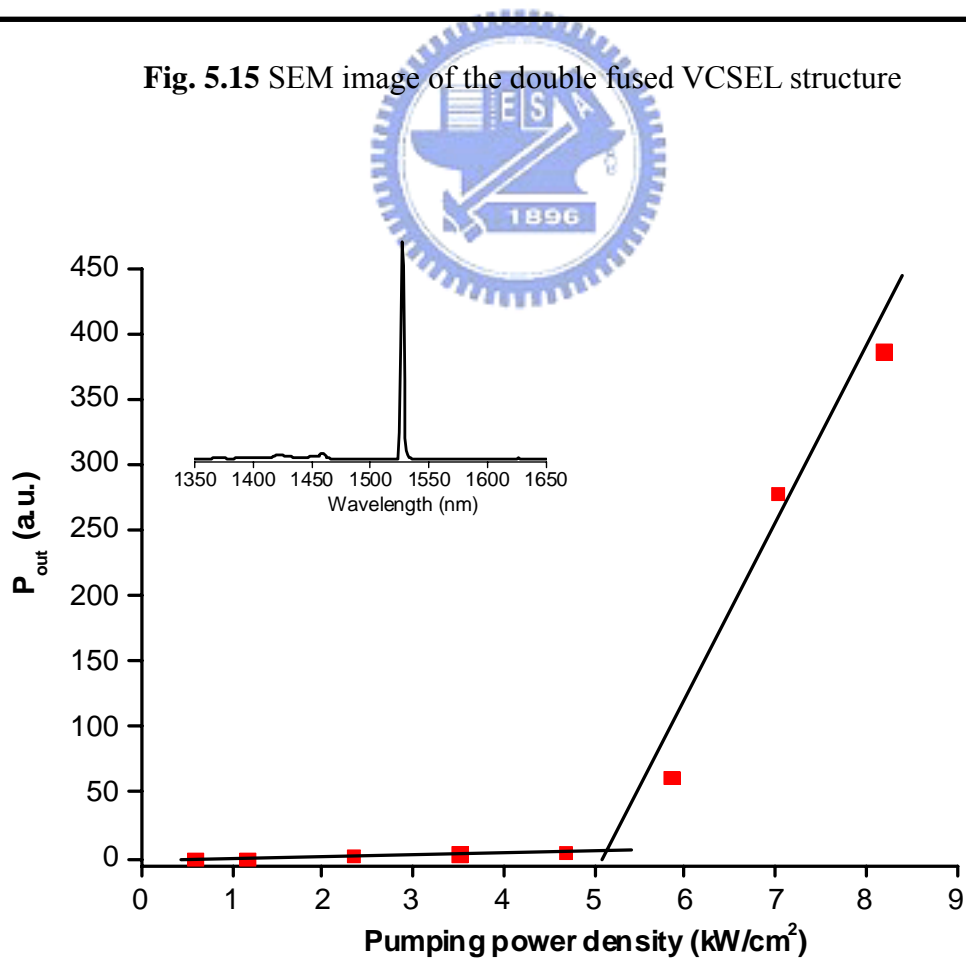
**Fig.5.14** Process flow chart of double fused VCSEL
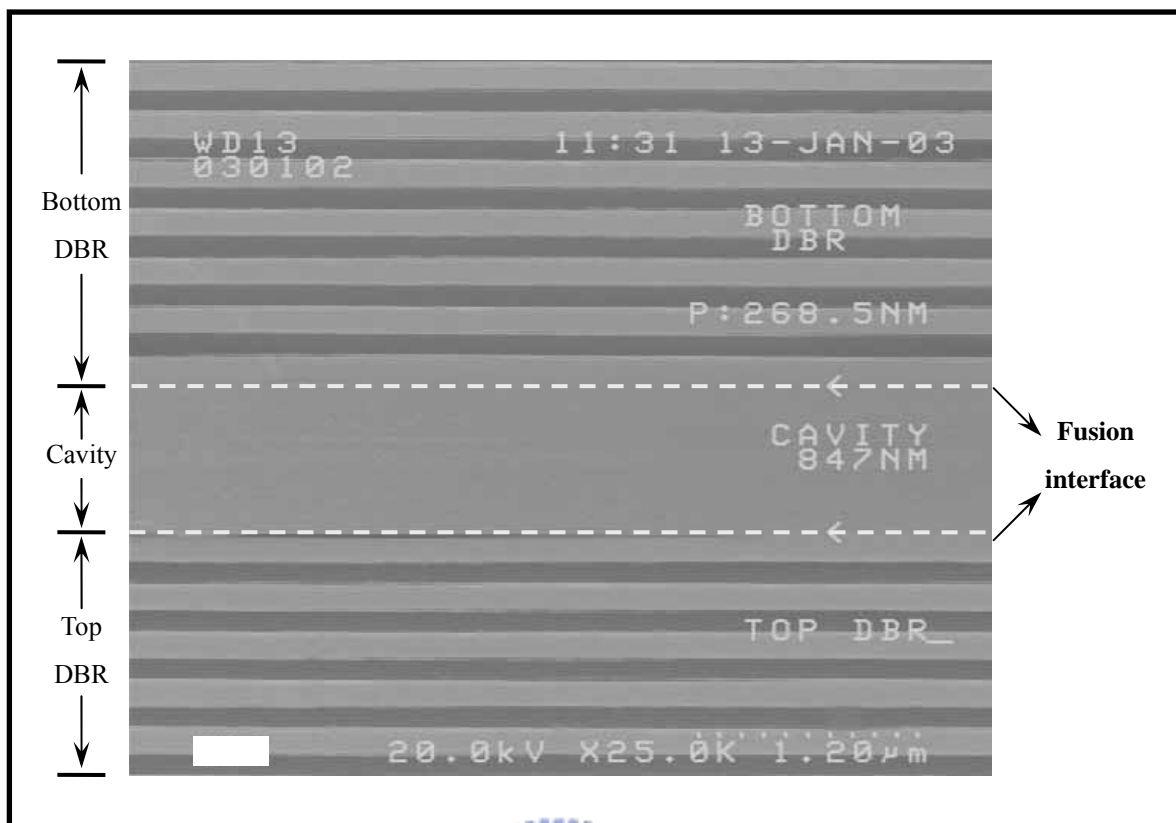
**Fig. 5.15** SEM image of the double fused VCSEL structure



**Fig. 5.16** The double fused VCSEL output power versus input pumping laser power density characteristics at room temperature

# Chapter 6 Conclusion

We have setup a wafer fusion system. The wafer fusion techniques and process conditions have been established. Smooth fusion interfaces has been observed with cross-section SEM images. 450°C is the proper fusion temperature for well fused fusion interface and low resistance across fused n-InP / n-GaAs heterojunction.

After experienced fusion process, the crystal quality of InGaAlAs MQW do not degrade. The reflectance spectra, stop band and maximum reflectivity of GaAs/AlAs DBR before and after fusion process do not change.

A VCSEL structure consists of InGaAlAs MQW, a fused 25 pairs GaAs/AlAs DBR and 10 pairs $SiO_2/TiO_2$ top dielectric mirror has been demonstrated. The optically pumped single fused VCSELs operated at room temperature with the threshold pumping power density of 4.5 $kW/cm^2$ and emitted laser at 1623.5nm.

We also demonstrated the optically pumped VCSEL structure with the fused bottom 30 pairs GaAs/AlAs DBR, InGaAlAs MQW and the fused top 25 pairs GaAs/AlAs DBR. The optically pumped double fused VCSELs operated at room temperature with the threshold pumping power density of 5 $kW/cm^2$ and emitted laser at 1527nm.

In conclusion, wafer fusion is an applicable and potential technique for fabrication of LW-VCSEL using GaAs/AlAs as DBR mirrors.In the future, optimum design of the active region and DBR are necessary. The double fused VCSEL with

doped GaAs/AlAs DBR is planed to be demonstrated. Electrically driven VCSEL is the next step after the success of optically pumped VCSEL.

# Reference

[1.1] "Properties of Indium Phosphide", EMIS atareviews Series, No.6.
( INSPEC, London, 1991) .

[1.2] T. Baba, Y. Yogo, K. Suzuki, F. Koyama, and K. Iga, Electron. Lett. 29, 913 (1993).

[1.3] K. Uomi, S. J. B. Yoo, A. Scherer, R. Bhat, N. C. Andredakis, C. E. Zah, M. A. Koza, and T. P. Lee, IEEE Photonics Technol. Lett. 6, 317 (1994).

[1.4] J. J. Dudley, D. I. Babic, R. Mirin, L. Yang, B. I. Miller, R. J. Ram, T. E. Reynolds, E. L. Hu, and J. E. Bowers, Appl. Phys. Lett. 64, 1463 (1994).

[1.5] Z. L. Ziao and D. E. Mull, Appl. Phys. Lett. 56, 737 (1990).

[1.6] Y. H. Lo, R. Bhat, D. M. Koza, and T. P. Lee, Appl. Phys. Lett. 58, 1961 (1991).

[1.7] R. J. Ram, L. Yang, K. Nauka, Y. M. Huong, M. Ludowise, D. E. Mars, J.J. Dudley, and S. Y. Wang, Appl. Phys. Lett. 62, 2474 (1993).

[1.8] I-H. Tan, J. J. Dudley, D. I. Babic, D. A. Cohen, B. D. Young, E. L. Hu, J.E. Bowers, B. I. Miller, U. Koren, and M. G. Young, IEEE Photonics Technol. Lett. 6, 811 (1994).

[2.1-3] L.A. Coldren, S.W. Corzine, *"Diode laser and photonic integrated circuits"*, John Wiley and Sons (1995)

[2.4] *Properties of Indium Phosphide*, EMIS Datareviews Series, No. 6.(INSPEC, London, 1991).

[2.5] Paul H. Holloway and Gary E. McGuire *"Handbook of compound semiconductors"* Park Ridge, NJ /Noyes

[3.1] F. E. Ejeckam, C. L. Chua, Z. H. Zhu, Y. H. Lo, M. Hong, and R. Bhat, Appl. Phys. Lett. 67, 3936 (1995).

[3.2] A. R. Hawkins, W. Wu, P. Abraham, K. Streubel, and J. E. Bowers, Appl. Phys. Lett. 70, 303 (1997).

[3.3] J. J. Dudley, D. I. Babic, R. Mirin, L. Yang, B. I. Miller, R. J. Ram, T. Reynolds, E. L. Hu, and J. E. Bowers, Appl. Phys. Lett. 64, 1463 (1994).

[3.4] D. I. Babic, J. J. Dudley, K. Streubel, R. P. Mirin, J. E. Bowers, and E. L. Hu, Appl. Phys. Lett. 66, 1030 (1995).

[3.5] I.-H. Tan, J. J. Dudley, D. I. Babic, D. A. Coldren, B. D. Young, E. L. Hu, J. E. Bowers, B. I. Miller, U. Koren, and M. G. Young, IEEE Photonics Technol. Lett. 6, 811 (1994).

[3.6] F. A. Kish, F. M. Steranka, D. C. DeFevere, D. A. Vanderwater, K. G. Park, C. P. Kuo, T. D. Osentowski, M. J. Peannasky, J. G. Yu, R. M. Fletcher, D. A. Steigwald, M. G. Craford, and V. M. Robbins, Appl. Phys. Lett. 64, 2839(1994).

[3.7] G. E. Hofler, D. A. Vanderwater, D. C. DeFevere, F. A. Kish, M. D. Camras, F.

M. Steranka, and I.-H. Tan, Appl. Phys. Lett. 69, 803 (1996).

[3.8] Z. L. Liua, J. N. Walpole, and D. Z. Tsang, IEEE J. Quantum Electron. QE-20, 855(1984).

[3.9] Y. H. Lo, R. Bhat, D. M. Hwang, M. A. Koza, and T. P. Lee, Appl. Phys. Lett. 58, 1961 (1991).

[3.10] K. Miro, K. Tokutome, K. Nishi, and S. Sugou, Electron. Lett. 30, 1008 (1994).

[3.11] A. V. Syrbu, J. Fernandez, J. Behrend, C. A. Berseth, J. F. Carlin, A. Rudra, and E. Kapon, Electron. Lett. 33, 866 (1997).

[3.12] D. I. Babic, K. Streubel, R. P. Mirin, N. M. Margalit, J. E. Bowers, E. L. Hu, D. E. Mars, L. Yang, and K. Carey, IEEE Photonics Technol. Lett. 7, 1225 (1995).

[3.13] Y. Ohiso, C. Amano, Y. Itoh, K. Tateno, T. Tadokoro, H. Takenouchi, and T. Kurokawa, Electron. Lett. 32, 1483 (1996).

[3.14] N. M. Margalit, D. I. Babic, K. Streubel, R. P. Mirin, R. L. Naone, J. E. Bowers, and E. L. Hu, Electron. Lett. 32, 1675 (1996).

[3.15] E. Yablonovitch, D. M. Hwang, T. J. Gmitter, L. T. Florez, and J. P. Harbison Appl. Phys. Lett. 58, 2419 (1990)

[3.16] TaekRyong Chung, Naoe Hosoda, and Tadatomo Suga, Appl. Phys. Lett. 72, 1565 (1997)

[3.17] M. Shimbo, K. Furukawa, K. Fukuda, and K. Tanzawa, J. Appl. Phsic., 60, 2987 (1986)

[4.1] L.A. Coldren, S.W. Corzine, *"Diode laser and photonic integrated circuits"*, John Wiley and Sons (1995)

[5.1] M.Hammar, F. Wennekes 10th Intern. Conf. on Indium Phosphide and Related Materials "Systematics of electronical conductivity across InP to GaAs Wafer fused interfaces" (1998)

[5.2] D.I. Babic, PH.D. dissertion, University of California, Santa Babara, 1995.

[5.3] L.A. Coldren, S.W. Corzine, *"Diode laser and photonic integrated circuits"*, John Wiley and Sons (1995)